The Scattering and Intrinsic Structure of Sagittarius A* at Radio Wavelengths

Document Version
Final published version

[Link to publication record in Manchester Research Explorer](#)

OPEN ACCESS

The Scattering and Intrinsic Structure of Sagittarius A* at Radio Wavelengths

Michael D. Johnson[1], Ramesh Narayan[1], Dimitrios Psaltis[2], Lindy Blackburn[1], Yuri Y. Kovalev[3,4,5], Carl R. Gwinn[6], Guang-Yao Zhao[7], Geoffrey C. Bower[8], James M. Moran[1], Motoki Kino[9,10], Michael Kramer[5,11], Kazunori Akiyama[12], Jason Dexter[13], Avery E. Broderick[14,15], and Lorenzo Sironi[16]

[1] Harvard-Smithsonian Center for Astrophysics, 60 Garden Street, Cambridge, MA 02138, USA; mjohnson@cfa.harvard.edu
[2] Astronomy Department, University of Arizona, 933 N. Cherry Ave, Tucson, AZ 85721, USA
[3] Astro Space Center of Lebedev Physical Institute, Profsoyuznaya 84/32, 117997 Moscow, Russia
[4] Moscow Institute of Physics and Technology, Institutsky per. 9, Dolgoprudny 141700, Russia
[5] Max-Planck-Institut für Radioastronomie, Auf dem Hügel 69, D-53121 Bonn, Germany
[6] Department of Physics, University of California, Santa Barbara, CA 93106, USA
[7] Korea Astronomy and Space Science Institute, Daedeok-daero 776, Yuseong-gu, Daejeon 34055, Republic of Korea
[8] Academia Sinica Institute of Astronomy and Astrophysics, 645 N. A'ohoku Place, Hilo, HI 96720, USA
[9] Kogakuin University of Technology & Engineering, Academic Support Center, 2665-1 Nakano, Hachioji, Tokyo 192-0015, Japan
[10] National Astronomical Observatory of Japan, 2-21-1 Osawa, Mitaka, Tokyo, 181-8588, Japan
[11] Jodrell Bank Centre for Astrophysics, The University of Manchester, Manchester M13 9PL, UK
[12] Massachusetts Institute of Technology, Haystack Observatory, Route 40, Westford, MA 01886, USA
[13] Max Planck Institute for Extraterrestrial Physics, Giessenbachstr. 1, D-85748 Garching, Germany
[14] Perimeter Institute for Theoretical Physics, 31 Caroline Street North, Waterloo, ON N2L 2Y5, Canada
[15] Department of Physics and Astronomy, University of Waterloo, 200 University Avenue West, Waterloo, ON N2L 3G1, Canada
[16] Department of Astronomy, Columbia University, 550 W 120th St, New York, NY 10027, USA

Abstract

Radio images of the Galactic Center supermassive black hole, Sagittarius A* (Sgr A*), are dominated by interstellar scattering. Previous studies of Sgr A* have adopted an anisotropic Gaussian model for both the intrinsic source and the scattering, and they have extrapolated the scattering using a purely λ^2 scaling to estimate intrinsic properties. However, physically motivated source and scattering models break all three of these assumptions. They also predict that refractive scattering effects will be significant, which have been ignored in standard model fitting procedures. We analyze radio observations of Sgr A* using a physically motivated scattering model, and we develop a prescription to incorporate refractive scattering uncertainties when model fitting. We show that an anisotropic Gaussian scattering kernel is an excellent approximation for Sgr A* at wavelengths longer than 1 cm, with an angular size of $(1.380 \pm 0.013)\lambda_{\rm cm}^2$ mas along the major axis, $(0.703 \pm 0.013)\lambda_{\rm cm}^2$ mas along the minor axis, and a position angle of $81°9 \pm 0°2$. We estimate that the turbulent dissipation scale is at least 600 km, with tentative support for $r_{\rm in} = 800 \pm 200$ km, suggesting that the ion Larmor radius defines the dissipation scale. We find that the power-law index for density fluctuations in the scattering material is $\beta < 3.47$, shallower than expected for a Kolmogorov spectrum ($\beta = 11/3$), and we estimate $\beta = 3.38^{+0.08}_{-0.04}$ in the case of $r_{\rm in} = 800$ km. We find that the intrinsic structure of Sgr A* is nearly isotropic over wavelengths from 1.3 mm to 1.3 cm, with a size that is roughly proportional to wavelength: $\theta_{\rm src} \sim (0.4~{\rm mas}) \times \lambda_{\rm cm}$. We discuss implications for models of Sgr A*, for theories of interstellar turbulence, and for imaging Sgr A* with the Event Horizon Telescope.

Key words: Galaxy: nucleus – ISM: structure – radio continuum: ISM – scattering – techniques: interferometric – turbulence

1. Introduction

The compact radio source at the Galactic Center, Sagittarius A* (Sgr A*), was discovered in 1974 (Balick & Brown 1974). Within two years, observers had deduced that the radio image was dominated by scatter broadening caused by the ionized interstellar medium (ISM) based on an observed scaling of image size with the squared observing wavelength, $\theta \propto \lambda^2$ (Davies et al. 1976). In the decades since the initial discovery of Sgr A*, knowledge of its scattering properties has continually improved, but scattering uncertainties remain the primary limitation in determining its intrinsic structure at wavelengths longer than a few millimeters.

Motivated by the $\theta \propto \lambda^2$ scaling and approximately Gaussian image, many observers have sought to accurately measure the image of Sgr A* at a wide range of radio wavelengths, seeking to constrain the scattering law at long wavelengths (where the scattering dominates) and then to deconvolve its effects at shorter wavelengths to estimate the

intrinsic source parameters. An advantage of treating both the source and the scattering as Gaussian is that the scattered image is then also a Gaussian because the time-averaged scattering acts as a convolution (see, e.g., Coles et al. 1987; Goodman & Narayan 1989; Johnson & Gwinn 2015). Consequently, many techniques have been developed to accurately estimate Gaussian image parameters for Sgr A* from interferometric data, including image-domain parameter estimation (Bower et al. 2006), model fitting using only closure quantities (Bower et al. 2004, 2014b; Shen et al. 2005; Brinkerink et al. 2016; Ortiz-León et al. 2016), and self-calibration (Doeleman et al. 2001; Lu et al. 2011; Ortiz-León et al. 2016). In addition, many techniques have been applied to ensure conservative estimates of parameter uncertainty, including standard exploration of the chi-squared hypersurface (e.g., Bower et al. 2014b), Monte Carlo approaches (Ortiz-León et al. 2016), and bootstrap approaches using multi-epoch data (e.g., Lu et al. 2011). Nevertheless, the

reported sizes and position angles still have significant unresolved discrepancies (see Psaltis et al. 2015b).

In addition to the simplified scattering model, a major missing component from all these previous studies has been refractive scattering effects. Refractive scattering will distort the instantaneous image, giving systematic departures from the ensemble-average image that are independent of observing quality (Blandford & Narayan 1985). Refractive scattering also introduces substructure in the image, which contributes additional "refractive noise" to interferometric measurements on baselines that resolve the image (Goodman & Narayan 1989; Narayan & Goodman 1989; Johnson & Gwinn 2015). Recently, refractive noise was discovered in 1.3 cm observations of Sgr A* (Gwinn et al. 2014), suggesting that it may contribute significantly to the error budget when fitting Gaussian models. Refractive noise is especially problematic because the longer baselines, which are most affected, are also the most sensitive to compact structure; their measurements are what dominate Gaussian model fits. Because refractive noise tends to bias long-baseline visibility amplitudes upward, detections interpreted without a noise budget for refractive substructure will tend to imply artificially compact structure (see, e.g., Johnson et al. 2016; Pilipenko et al. 2018). Thus, refractive scattering effects are essential to include when fitting models to interferometric data, and they contribute in multiple ways, both by modulating the "true" instantaneous image size and orientation and by adding a new type of "noise" to interferometric measurements.

Here, we analyze archival observations of Sgr A* at wavelengths from 1.3 mm (Event Horizon telescope, EHT) to 30 cm (Very Large Array, VLA). We develop a framework to efficiently incorporate refractive noise into parametric model fitting, and we show how to isolate components of the refractive noise that may be absorbed into fitted model parameters (e.g., refractive flux modulation and image wander). We constrain a physically motivated scattering model (Psaltis et al. 2018), which generically produces Gaussian scatter-broadening that scales as λ^2 in the limit $\lambda \to \infty$, but which differs at short wavelengths because of a finite inner scale $r_{\rm in}$ of the interstellar turbulence with an associated power-law index α. In addition to these two parameters, the scattering model depends on the Gaussian scatter broadening in the long-wavelength limit, which we parameterize via the major axis full width at half maximum (FWHM) $\theta_{\rm maj,0}$, minor axis FWHM $\theta_{\rm min,0}$, and major axis position angle $\phi_{\rm PA}$, all specified at a reference wavelength λ_0 (we use $\lambda_0 \equiv 1$ cm).

We estimate uncertainties in our parameter estimates by fitting representative ensembles of synthetic data sets that match the baseline coverage and sensitivity of the observations. These synthetic data sets are created using numerical simulations of the scattering and also include wavelength-dependent systematic gain calibration uncertainties to simulate imperfect amplitude and phase calibration. This approach allows us to incorporate thermal noise, refractive uncertainties, and systematic calibration errors in the overall error budget, and to verify that our model fitting is not biased by any of these effects or by the anisotropic baseline coverage. Using our estimated scattering model, we compute the wavelength-dependent intrinsic size of Sgr A*.

We begin, in Section 2, with a brief review of scattering theory. Next, in Section 3, we describe our procedure to fit individual observations and motivate how we can use the full set of observations to constrain the scattering model. In Section 4, we provide details about the observations used to constrain the scattering model and give the results of Gaussian fits to each. In Section 5, we derive our parameter estimates and uncertainties for the scattering model, describe the expected scattering properties, and estimate the intrinsic source size of Sgr A*. In Section 6, we discuss implications for models of Sgr A*, implications for theories of interstellar turbulence, consequences of unmet assumptions in our approach, and prospects for continued study of Sgr A*. We summarize our findings in Section 7.

2. Scattering Model

2.1. Background

The basic properties of interstellar scattering have been summarized in several reviews (e.g., Rickett 1990; Narayan 1992; Thompson et al. 2017), and our specific scattering model is derived and discussed in detail in a companion paper (Psaltis et al. 2018). Here, we will only briefly summarize the key properties that are of immediate relevance for the remainder of this paper.

Interstellar scattering and scintillation at radio wavelengths is caused by density inhomogeneities in the ionized ISM. Neglecting a weak birefringence from the magnetic field (which is negligible for the observing wavelengths we consider), the local index of refraction of the ISM is given by $n \approx 1 - \frac{1}{2}\left(\frac{\nu_{\rm p}}{\nu}\right)^2$, where ν is the wave frequency, $\nu_{\rm p} \approx 9.0 \times \sqrt{\frac{n_{\rm e}}{1\,{\rm cm}^{-3}}}$ kHz is the plasma frequency, and $n_{\rm e}$ is the electron density (see, e.g., Thompson et al. 2017). A density fluctuation $\delta n_{\rm e}$ along a path length dz then introduces a corresponding phase change $\delta\phi = -r_{\rm e}\lambda \times dz \times \delta n_{\rm e}$, where $r_{\rm e} \approx 2.8 \times 10^{-13}$ cm is the classical electron radius and λ is the wavelength. Note that this dispersion relation is quite general and is independent of a specific ISM scattering model or geometry.

Along many lines of sight, the effects of scattering can be approximated via a single thin phase screen $\phi(\boldsymbol{r})$, where $\boldsymbol{r}$ is a two-dimensional vector transverse to the line of sight. Electron density fluctuations imprint their spectrum on the power spectrum $Q(\boldsymbol{q})$ of phase fluctuations, which are typically characterized by a single, unbroken power law between some outer ($r_{\rm out}$) and inner ($r_{\rm in}$) scales: $Q(\boldsymbol{q}) \propto |\boldsymbol{q}|^{-\beta}$. This description is expected for a top-down turbulent cascade between an injection scale and a dissipation scale, and a Kolmogorov spectrum of density fluctuations gives $\beta = 11/3$ (Goldreich & Sridhar 1995).

The effects of scattering on interferometric measurements are conveniently characterized using the phase structure function of the scattering screen, $D_\phi(\boldsymbol{r}) \equiv \langle[\phi(\boldsymbol{r}' + \boldsymbol{r}) - \phi(\boldsymbol{r}')]^2\rangle \propto \lambda^2$. In the ensemble-average scattering limit (see Goodman & Narayan 1989; Narayan & Goodman 1989), the effects of scattering are to convolve an unscattered image with a scattering kernel or, equivalently, to multiply unscattered interferometric visibilities by the appropriate Fourier-conjugate kernel. This kernel is given by $\exp\left[-\frac{1}{2}D_\phi(\boldsymbol{b}/(1 + M))\right]$, where $\boldsymbol{b}$ is the vector baseline of the interferometer and $M = D/R$ is the "magnification" of the scattering screen (D is the observer–screen distance; R is the source–screen distance). For spatial displacements smaller than $r_{\rm in}$, the phase fluctuations will be smooth, $\phi(\boldsymbol{r}' + \boldsymbol{r}) \approx \phi(\boldsymbol{r}') + \boldsymbol{r} \cdot \vec{\nabla}\phi(\boldsymbol{r}')$. In this

limit, $D_\phi(\boldsymbol{r}) \propto r^2\lambda^2$ (Tatarskii 1971). This expression—which makes no assumptions other than the cold plasma dispersion relation and smoothness of phase fluctuations below some scale—shows that ensemble-average scatter-broadening should act as a (possibly anisotropic) Gaussian blurring that scales as $\theta_{\rm scatt} \propto \lambda^2$ for baselines $\boldsymbol{b} \lesssim (1 + M)r_{\rm in}$ (i.e., on angular scales $\theta \gtrsim \lambda/((1 + M)r_{\rm in})$. Moreover, because the time-averaged scattering kernel from an ensemble of thin screens is determined by the cumulative convolution of all the individual screens, this generic asymptotic behavior is not limited to thin-screen scattering. At longer baselines, $D_\phi(\boldsymbol{r}) \propto |\boldsymbol{r}|^\alpha$, where $\alpha \equiv \beta - 2$, and the corresponding image becomes non-Gaussian. In this regime, the angular broadening scales as $\theta_{\rm scatt} \propto \lambda^{1+\frac{2}{\alpha}}$ and the interferometric scattering kernel falls as $e^{-|\boldsymbol{b}|^\alpha}$. However, note that $D_\phi(\boldsymbol{r}) \propto \lambda^2$ regardless of α or the scattering model.

While scatter broadening is produced by phase fluctuations on the diffractive scale[17] $r_{\rm diff} \sim \lambda/((1 + M)\theta_{\rm scatt})$, refractive scintillation is dominated by modes that are comparable to the refractive scale (i.e., the projected size of angular broadening on the scattering screen): $r_{\rm ref} \sim \theta_{\rm scatt}D$. The Fresnel scale $r_{\rm F} \equiv \sqrt{\frac{DR}{D+R}\frac{\lambda}{2\pi}}$, which is defined entirely by geometrical parameters of the scattering, corresponds to the geometric mean of the diffractive and refractive scales. When $r_{\rm ref} > r_{\rm F} > r_{\rm diff}$, the scattering is said to be "strong" (e.g., the scattering of Sgr A* is strong for all frequencies lower than a few THz). In this case, refractive effects are most naturally described using the power spectrum of phase fluctuations: $Q(\boldsymbol{q}) \equiv (2\pi)^2\lambda^{-2}\int d^2\boldsymbol{r} \langle \phi(\boldsymbol{r'} + \boldsymbol{r})\phi(\boldsymbol{r})\rangle e^{-i\boldsymbol{q}\cdot\boldsymbol{r}}$. In this expression, the prefactor renders $Q(\boldsymbol{q})$ independent of wavelength.

To describe a full scattering model then requires six parameters. Three are needed to characterize the long-wavelength behavior (Gaussian scatter broadening with a λ^2 dependence). As described before, we use the FWHM along the major and minor axes at a reference wavelength and the major axis position angle: $\theta_{\rm maj,0}$, $\theta_{\rm min,0}$, and $\phi_{\rm PA}$. In addition, the power-law index α, inner scale $r_{\rm in}$, and outer scale $r_{\rm out}$ are needed. Psaltis et al. (2018) show how to compute the phase structure function, power spectrum, and scattering properties once these parameters are specified.

We caution that the exact specification of these parameters is not unique, and the radio scattering literature is particularly inconsistent in defining the inner scale. For example, Rickett (1990) and Smirnova & Shishov (2010) taper the power spectrum by $e^{-q^2r_{\rm in}^2}$, Coles et al. (1987) and Armstrong et al. (1995) use $e^{-q^2r_{\rm in}^2/2}$, Lambert & Rickett (1999) use $e^{-q^2r_{\rm in}^2/4}$, and Spangler & Gwinn (1990) use $e^{-qr_{\rm in}/(2\pi)}$. We use a power spectrum taper of the form $e^{-q^2r_{\rm in}^2}$.

2.2. Refractive Noise

Refractive scattering modes introduce many types of stochastic effects. They modulate the total flux density of an image, displace its centroid, and distort the overall image. They also introduce image substructure, even on scales for which the unscattered source was smooth. All of these effects introduce a new type of "noise" for interferometric measurements. This refractive noise has a fractional bandwidth of order unity and varies slowly, on the refractive timescale $t_{\rm ref} = r_{\rm ref}/V_\perp$,

---

[17] Formally, the diffractive scale is defined by $D_\phi(r_{\rm diff}) \equiv 1$.

where $V_\perp$ is the characteristic relative transverse velocity of the observer, scattering, and source. At centimeter wavelengths, Sgr A* has $r_{\rm ref} \approx (2 \times 10^{13} \text{ cm}) \times \lambda_{\rm cm}^2$. Taking $V_\perp \sim 50 \text{ km s}^{-1}$ gives $t_{\rm ref} \sim (50 \text{ days}) \times \lambda_{\rm cm}^2$.

Johnson & Gwinn (2015) and Johnson & Narayan (2016) provide expressions for how to compute properties of refractive noise, including the variance of refractive fluctuations of a complex visibility measured on a vector baseline $\boldsymbol{b}$: $\sigma_{\rm ref}^2(\boldsymbol{b}) \equiv \langle|\Delta V(\boldsymbol{b})|^2\rangle$. However, for short baselines, this variance is not the correct quantity to apply to standard very long baseline interferometry (VLBI) analyses. Namely, part of the variance is due to variations in the total flux density, caused by refractive focusing, and part is due to image wander, caused by refractive deflections. Both of these effects would be eliminated in a typical VLBI analysis. The flux variations would be absorbed into the estimated total source flux density, and the image wander would be eliminated by centering the image (since VLBI has no concept of absolute position without absolute phase referencing).

Appendix A shows how to compute a *renormalized* visibility variance, $\hat{\sigma}_{\rm ref}(\boldsymbol{b})$, that eliminates these contributions. For example, the renormalized refractive noise is zero in the limit of zero baseline. On short baselines, it is dominated by changes in the overall image size from scattering—a property that we utilize in Section 5.2.2. We will include renormalized refractive noise in the error budget for our model fitting.

2.3. Assumed Scattering Properties of Sgr A*

We will use a few supplementary measurements and assumptions about the scattering of Sgr A*. The first is for the scattering geometry of Sgr A*. Because the Galactic Center magnetar lies only 2$\farcs$4 from Sgr A* (Bower et al. 2015a), its radio pulsations permit an estimate of temporal broadening associated with the scattering toward Sgr A*. This measurement can be combined with the angular broadening to estimate the location of the scattering material (Gwinn et al. 1993). For instance, if the scattering is isotropic, then the pulse-broadening function is exponential: $g(t) = e^{-t/\tau}$. This expression follows by relating a radial distance r on the scattering screen to its corresponding geometric delay, $t(r) \approx \frac{r^2}{2c}\left(\frac{1}{D} + \frac{1}{R}\right)$, and then expressing the brightness distribution on the sky in terms of t. The $1/e$ scale of the temporal broadening, τ, is related to the FWHM angular size of the scattered image, $\theta_{\rm scatt}$, via (e.g., Cordes & Lazio 1997)

$$c\tau = \frac{Md_{\rm src}}{8\ln(2)}\theta_{\rm scatt}^2, \tag{1}$$

where $d_{\rm src} = D + R$ is the distance from the observer to the source, and $M = D/R$. Because the magnetar shows angular broadening comparable to Sgr A*, the same scattering material is thought to dominate the angular broadening of each (Bower et al. 2014a, 2015a). The temporal broadening of the magnetar can then be combined with the angular broadening and distance to Sgr A* to estimate the location of the scattering material for both objects.

For anisotropic scattering, the pulse-broadening function is monotonically decreasing but not exponential. For a scattered image with FWHM $\theta_{\rm maj}$ and $\theta_{\rm min}$ along the major and minor

axes, the pulse-broadening function takes the form[18]

$$g(t) = I_0 \left(\frac{4 \ln(2) ct}{M d_{\text{src}} \theta_-^2} \right) e^{-\frac{4 \ln(2) ct}{M d_{\text{src}} \theta_+^2}},$$

$$\theta_\pm \equiv \frac{\theta_{\text{maj}} \theta_{\text{min}}}{\sqrt{\theta_{\text{maj}}^2 \pm \theta_{\text{min}}^2}}. \qquad (2)$$

In this case, determining τ (i.e., solving $g(\tau) = g(0)/e$) must be done numerically.

We will assume a distance to Sgr A* of 8.1 kpc (Gravity Collaboration et al. 2018). Using our estimated scattering kernel parameters (see, e.g., Table 2), we obtain $\tau_{1\,\text{GHz}}/(1\,\text{s}) \approx 2.47M$. Using the measured value $\tau_{1\,\text{GHz}} = 1.3 \pm 0.2$ s (Spitler et al. 2014) then gives $M = 0.53 \pm 0.08$. Note that this estimate differs slightly from the simpler approach of using the isotropic scattering result with the geometric mean of the major and minor scattering axes, which gives $\tau_{1\,\text{GHz}}/(1\,\text{s}) \approx 2.77M$ (Bower et al. 2014a). Using the exact expression for anisotropic scattering, we obtain $D = 2.7$ kpc and $R = 5.4$ kpc.

There is now compelling evidence that at least some of the temporal broadening of the magnetar is local to the Galactic Center region (see, e.g., Dexter et al. 2017; Desvignes et al. 2018). Because angular broadening is more sensitive to scattering material closer to the observer, it is likely that the angular broadening and refractive effects are dominated by the scattering region that is distant from the Galactic Center. Because the temporal broadening caused by this material may be smaller than the value used above, the corresponding M for the scattering responsible for the angular broadening may be somewhat *lower* and the scattering material somewhat further from the Galactic center. However, our later results are insensitive to changes in M. Refractive noise scales as $\sigma_{\text{ref}} \propto M^{-1 + \frac{\alpha}{2}}$ (e.g., $\sigma_{\text{ref}} \propto M^{-1/6}$ for a Kolmogorov spectrum), while our later inner scale constraint is proportional to $(1 + M)^{-1}$. Thus, even a change in our assumed temporal broadening by a factor of 2 would not strongly affect our conclusions, and so we will work within the single-screen framework for the remainder of this paper.

Our second assumption is that the outer scale for the scattering of Sgr A* is sufficiently large to be irrelevant for our calculations (specifically, we require $r_{\text{out}} \gg 10$ au). We will discuss the validity of this assumption in Section 6.2.1.

3. Scattering Model Fitting Procedure

We now describe our procedure to fit observations, constrain the full scattering model, and estimate parameter uncertainties. Our fitting strategies are guided by synthetic data sets. We generated data sets with identical baseline coverage and sensitivity to our actual observations of Sgr A*, but with visibilities generated from simulated scattered images. We use a Monte Carlo approach to determine our uncertainties, fitting an ensemble of synthetic observations of scattered images. Thus, our reported uncertainties account for thermal noise, limitations of the fitting procedure, and systematic uncertainties from refractive scattering.

---

[18] Rickett et al. (2009) and Gwinn et al. (2016) derive similar expressions for g (*t*). However, note that Rickett et al. (2009) express their results in terms of the scattering angle of the screen θ_s rather than the observed scattering angle $\theta = R(D + R)^{-1}\theta_s = (1 + M)^{-1}\theta_s$.

3.1. Anisotropic Gaussian Model Assumption

One significant simplification in our model fitting approach is that we model the brightness distribution of the source on the sky as a wavelength-dependent anisotropic Gaussian. In Section 2, we demonstrated that this assumption is well motivated for the shape of the scatter broadening because it corresponds to universal scattering behavior in the limit of long wavelength. Moreover, our approach to estimate parameter uncertainties uses the full, non-Gaussian scattering model, so our final error budget accounts for limitations in the assumption of Gaussian scatter broadening. However, the intrinsic source may be non-Gaussian, especially when the emission region becomes optically thin. Nevertheless, even in this regime, the Gaussian source assumption is well motivated for model fitting and has a meaningful associated FWHM, as we will now demonstrate.

Specifically, the interferometric visibility $\tilde{I}(\boldsymbol{u})$ on a short baseline $\boldsymbol{u}$ can be approximated as

$$\tilde{I}(\boldsymbol{u}) = \int d^2\boldsymbol{x}\, I(\boldsymbol{x})\, e^{-2\pi i \boldsymbol{u} \cdot \boldsymbol{x}}$$

$$\approx \int d^2\boldsymbol{x}\, I(\boldsymbol{x}) [1 - 2\pi i \boldsymbol{u} \cdot \boldsymbol{x} - 2\pi^2 (\boldsymbol{u} \cdot \boldsymbol{x})^2], \qquad (3)$$

where $I(\boldsymbol{x})$ denotes the image, with $\boldsymbol{x}$ an angular coordinate on the sky (Thompson et al. 2017). The term that is linear in $\boldsymbol{u}$ reflects an interferometric phase that is proportional to the image centroid projected along the baseline direction (from the Fourier shift theorem). Standard VLBI observations (including all those used in this paper) do not have absolute phase information, so we can set this term to zero (i.e., we use the image centroid to define the origin of the sky coordinates). The remaining terms in Equation (3) show that the visibility amplitude decreases quadratically with baseline length for short baselines. The quadratic coefficient is proportional to the second moment of the image projected along the baseline direction. This second moment can then be used to define a characteristic image FWHM, using the relationship corresponding to a perfectly Gaussian image. For example, the major axis FWHM θ_{maj} is given by

$$\theta_{\text{maj}} = \sqrt{-\frac{2 \ln(2)}{\pi^2 \tilde{I}(0)} \nabla_{\hat{\boldsymbol{u}}_{\text{maj}}}^2 \tilde{I}(\boldsymbol{u}) \rceil_{\boldsymbol{u}=0}}, \qquad (4)$$

where $\tilde{I}(0)$ is the total flux density of the image, and $\nabla_{\hat{\boldsymbol{u}}_{\text{maj}}}^2$ is the second directional derivative along the major axis direction. The three characteristic Gaussian parameters $\{\theta_{\text{maj}}, \theta_{\text{min}}, \phi\}$ can be determined by diagonalizing the image covariance matrix.

For this universal Gaussian behavior for the source visibility function to be applicable, the baselines must only marginally resolve the *unscattered* source. For Sgr A*, this assumption can be assessed post hoc using the inferred intrinsic size. Using the characteristic size $\theta_{\text{src}} \sim (0.4\,\text{mas}) \times \lambda_{\text{cm}}$ that we derive later (see Section 5.3), we estimate that projected baselines must have a length of approximately 3000 km for the normalized visibility function of the intrinsic source to fall to $1/e$ (this length is independent of wavelength because the source grows linearly with wavelength while angular resolution scales inversely with wavelength). For all observations we analyze other than 1.3 and 3.5 mm, the longest baselines are significantly shorter than this limit (because longer baselines

heavily resolve the *scattered* source). Thus, for the wavelengths we analyze to estimate the scattering kernel ($\lambda \geqslant 7$ mm), the quadratic expansion of Equation (3) and Gaussian approximation are well motivated for the intrinsic structure of Sgr A*.

3.2. Anisotropic Gaussian Fitting Procedure

To estimate the scattering kernel of Sgr A*, we independently fit anisotropic Gaussian models to observations of Sgr A* at wavelengths from 1.3 mm to 30 cm. In principle, fitting a Gaussian to interferometric data is quite simple. In practice, the fitting is subtle and subject to many sources of noise and bias. These include thermal noise, station-based systematic errors in amplitude and phase, and refractive noise. We developed a simplified prescription for Gaussian model fitting that accounts for all these errors. Our prescription is motivated by tests on synthetic data sets (see Section 3.3); it sacrifices some exactness for the sake of computational efficiency. Nevertheless, our approach provides a reliable error budget despite shortcomings in the model fitting procedure.

For each observation, we began with complex visibilities that had a priori amplitude calibration applied but no self calibration. We first flagged all visibilities for which the elevation at either station was below 5°. Next, on a scan-by-scan basis, we flagged all stations that did not have a signal-to-noise ratio (S/N) of at least 12 on any baseline. Thus, at each time, a station was only included if it had at least one strong fringe detection. This station-based cut was chosen to avoid including visibilities with a noise bias from the fringe search; a baseline-based cut would also avoid spurious fringes but would potentially bias the set of unflagged, low-S/N visibility amplitudes upward. Next, we computed the expected renormalized refractive noise (see Section 2.2) for each point, and eliminated all visibilities for which the ensemble-average visibility function was less than four times the renormalized refractive noise. This cut eliminated visibilities that were dominated by refractive noise from the Gaussian model fits (we only performed this final cut for the Gaussian model fitting and included these visibilities for estimates of the long-baseline refractive noise).

Next, we jointly fit for complex, time-dependent station gains at every site and the Gaussian image parameters (i.e., self-calibration to a model), seeking the maximum a posteriori estimate of all parameters. For this estimate, we used flat priors on the station phases and Gaussian priors on the logarithm of the gain amplitude, centered on a gain of amplitude of unity and with wavelength- and array-dependent spread. We used 5% uncertainty for VLA data at 15–30 cm, 5% uncertainty at 3.6 cm for Very Long Baseline Array (VLBA) data, and 10% uncertainty at 1.3 cm (VLBA) and 7 mm (Korean VLBI Network and VERA Array (KaVA)). At 3.5 mm, the a priori calibration is sufficiently poor that we do not constrain the gain amplitudes (similar to an analysis using only closure quantities). These values can be validated after fitting the actual data and were guided by the expected performance for each wavelength/array combination. We assumed that the visibilities had complex Gaussian random noise, with a standard deviation that was the quadrature sum of the measured thermal noise and the renormalized refractive noise. In this way, we included additional tolerance for visibility errors from refractive noise.

3.3. Synthetic Observations for Monte Carlo Uncertainty Estimates

To estimate uncertainties for the fitted parameters, we used a Monte Carlo approach. Namely, for each data set analyzed, we generated a representative ensemble of synthetic data sets and analyzed each using our procedure for the actual data. To create synthetic data sets, we scattered Gaussian source images using the `stochastic-optics` module of the EHT-imaging library (Chael et al. 2016; Johnson 2016). The source and scattering parameters were chosen to match the current best estimates in our iterative fitting procedure (see Section 3.4). We then sampled each scattered image on the observed (u, v) coordinates and added complex Gaussian noise that was equal to the measured thermal noise. Next, we injected two types of gain uncertainty to the measurements: (1) fluctuations of the station gains that were uncorrelated from scan to scan, and (2) an overall uncertainty in each station gain that was constant over the entire observation but different among the different synthetic data sets. Each of these gain errors was a Gaussian random variable with unit mean and wavelength-dependent uncertainty, matching the values given Section 3.2.

As a concrete example, a single realization of the simulated 1.3 cm VLBA data would have rapid jitter from thermal noise that was uncorrelated among all baselines and times, rapid station-based jitter from the gain errors (rms of $\sqrt{2} \times 10\%$ of each visibility amplitude), and a constant station-based error (rms of $\sqrt{2} \times 10\%$ of each visibility amplitude). For instance, all baselines to a particular antenna might be systematically underestimating the true flux density in one realization and overestimating in another. Each realization also produced an image with FWHM fluctuations from refractive image distortions and with additional noise on long baselines from refractive substructure.

To estimate our parameter uncertainties, we compute the rms of the parameter estimates from each simulated data set with respect to the true, ensemble-average parameter. Thus, our uncertainties account for thermal scatter in the model fitting, for systematic scatter from the refractive scattering, and for systematic errors and bias in the model fitting procedure.

Real data have additional imperfections that our simplified prescription does not capture, including bandpass errors, polarimetric leakage, and gain errors that are elevation dependent. However, the polarization of Sgr A* is negligible at cm wavelengths, and residual bandpass errors are small. As we will demonstrate, the dominant source of uncertainty for many of our measurements is refractive scattering, and our Monte Carlo approach fully accounts for this uncertainty.

3.4. Overall Fitting Strategy

As described in the previous sections, we independently fit Gaussian models to data at multiple frequencies. However, these fits used refractive noise corresponding to the scattering properties that are estimated using the full multi-frequency data set. Thus, our overall fitting procedure is iterative.

1. We fit Gaussian models to the 1.3 and 3.6 cm data. These fits require estimates of r_{in} and α to determine the refractive noise to include in the model fitting procedure and in the Monte Carlo uncertainty estimation via synthetic data. We assume that the scattering dominates the intrinsic size at these wavelengths (as is supported by the λ^2 scaling), so we use these fits to estimate the three

parameters that characterize the long-wavelength scattering behavior: $\theta_{\mathrm{maj},0}$, $\theta_{\mathrm{min},0}$, ϕ_{PA}.

2. Keeping $\theta_{\mathrm{min},0}$ and ϕ_{PA} fixed at the values obtained in step 1, we fit the 15–30 cm VLA data to obtain a tighter constraint on $\theta_{\mathrm{maj},0}$.

3. Having determined the three parameters of the long-wavelength ensemble-average image in steps 1 and 2, we use four additional pieces of evidence to constrain r_{in} and α.

   (a) The nearly perfect scaling of image size as λ^2 down to 1.3 cm and across the observing bandwidth at 1.3 cm, combined with constancy of position angle and image anisotropy over this frequency range. These properties suggest that scattering must dominate over intrinsic structure at all wavelengths longer than 1.3 cm and that the inner scale must exceed the diffractive scale at 1.3 cm.

   (b) The Gaussian scaling of visibility amplitude with baseline length at 1.3 cm and tentative non-Gaussian scaling of visibility amplitude with baseline length at 7 mm.

   (c) The magnitude of refractive visibility noise using long-baseline measurements at 1.3 cm and 3.6 cm, where the Gaussian image contribution is negligible.

   (d) An upper limit of 3% on image size fluctuations at 7 mm, as determined by historical data.

4. We then repeat steps 1–3 using the full scattering model ($\theta_{\mathrm{maj},0}$, $\theta_{\mathrm{min},0}$, ϕ_{PA}, α, r_{in}) estimated in the previous pass to estimate a new set of scattering parameters.

4. Observations and Gaussian Fits

We now provide details on the specific observations that we use to constrain our scattering model. While previous scattering studies have generally relied on compiling large sets of observations and then averaging across multiple epochs to reduce parameter uncertainties, we instead consider a small number of high-quality observations and analyze each with a full scattering error budget.

4.1. VLA Observations at 20 cm

The longest-wavelength observations we examine are with the Karl G. Jansky VLA. These observations span wavelengths from 15 to 29 cm. The recorded bandwidth was divided into 16 spectral windows, each 64 MHz. Of the 16 original windows, four were flagged by the VLA calibration pipeline in CASA. We analyzed each spectral window independently. For each, we averaged in frequency and in one minute intervals. Figure 1 shows representative baseline coverage for one spectral window.

The long-wavelength data are subject to a challenge for Gaussian model fitting that does not affect our other observations. Namely, short baselines measure significant flux density that is not associated with Sgr A*; it is diffuse emission from the local Galactic Center environment. To eliminate contributions from this emission, we imposed a minimum baseline length u_{min} for visibilities used in the Gaussian fits. On baselines longer than $\sim 50\,k\lambda$, we did not see any indications of contaminating emission (e.g., via non-zero closure phases). Thus, we repeated Gaussian fits using $u_{\mathrm{min}} = 60\,k\lambda$, $80\,k\lambda$, and $100\,k\lambda$, and we then used the scatter of these solutions as our estimate for the measurement uncertainty.
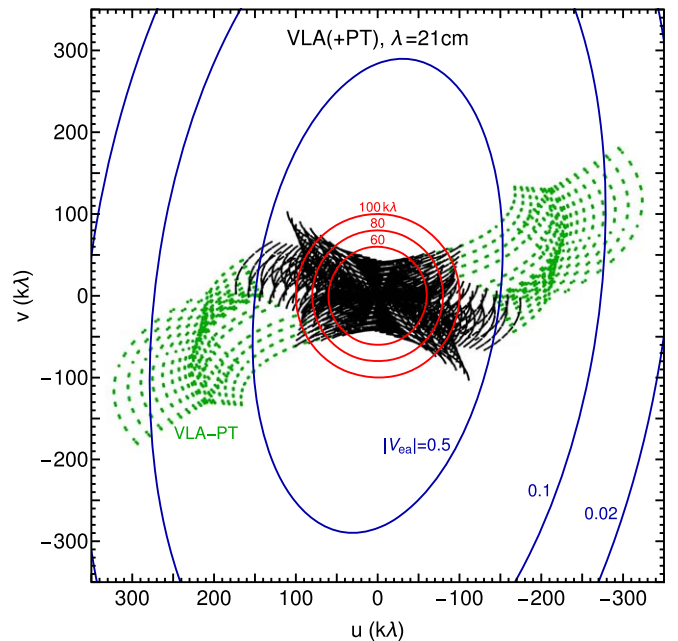

Figure 1. Baseline coverage of the VLA at the representative wavelength $\lambda = 21.06$ cm, with baselines to the single VLBA antenna at Pie Town in green. Red circles show our three cuts in $|\boldsymbol{u}|$ to eliminate flux density from diffuse emission near Sgr A*. Blue ellipses show contours at which the estimated ensemble-average Gaussian visibility function falls to 0.5, 0.1, and 0.02 of the zero-baseline value.

Because the VLA baselines only modestly resolve Sgr A*, we did not find stable results among the different spectral windows when fitting all Gaussian parameters separately. In addition, the fitted position angle was highly degenerate with the major axis size; smaller position angles produce a smaller major axis size because of the anisotropic baseline coverage (see Figure 1). To mitigate this problem, we instead fit the Gaussian parameters holding the minor axis and position angle fixed to the values determined by 3.6 and 1.3 cm observations (i.e., we only fit for the total flux density and major axis size in each spectral window). With this reduction, we obtained self-consistent estimates of the major axis among all spectral windows (see Table 1).

Fitting a single λ^2 scattering law to our measured major axis sizes yields $\theta_{\mathrm{maj},0} = 1.3799 \pm 0.0067$ mas. This uncertainty does not account for refractive scattering effects, and it underestimates thermal uncertainty because the measurements with varying u_{min} have identical thermal noise. The uncertainty in the assumed position angle, $\sigma_{\mathrm{PA}} \sim 0°.2$, gives an additional uncertainty of $\approx (0.004 \text{ mas}) \times (\sigma_{\mathrm{PA}}/1°)$, which is negligible. The uncertainty in the assumed minor axis is likewise negligible.

To estimate the total uncertainty, we repeated the Gaussian fits using multi-frequency sets of synthetic data generated from 10 simulated realizations of the scattering. For each realization, we estimated a scattering law from the fitted Gaussian parameters. Note that while these data do not include diffuse emission, we used the same procedure with cutoffs of $u_{\mathrm{min}} = 60\,k\lambda$, $80\,k\lambda$, and $100\,k\lambda$. These estimates of $\theta_{\mathrm{maj},0}$ had a scatter of 0.011 mas relative to the ensemble-average value for the simulations. This scatter accounts for refractive noise, thermal noise, and systematic noise from gain errors, but it does not account for systematic uncertainty from diffuse

Table 1
Summary of Elliptical Gaussian Fits to Sgr A*

λ cm	Instrument	Expt.	Obs. Date	θ_{maj} μas	θ_{min} μas	P.A. deg
28.84	VLA	15A-310	2015 Aug 20	1147000 ± 31000		
27.17	VLA	15A-310	⋯	1017000 ± 11000		
23.22	VLA+PT	AB1134	2004 Oct 1 and 4	664000 ± 121000		
22.05	VLA	15A-310	⋯	672000 ± 28000		
21.96	VLA+PT	AB1134	⋯	682000 ± 14000		
21.06	VLA	15A-310	⋯	609000 ± 16000		
20.89	VLA+PT	AB1134	⋯	624000 ± 4000		
20.15	VLA	15A-310	⋯	546000 ± 12000		
19.78	VLA+PT	AB1134	⋯	544000 ± 6000		
18.56	VLA	15A-310	⋯	489000 ± 6000		
18.00	VLA+PT	AB1134	⋯	464000 ± 12000		
17.85	VLA	15A-310	⋯	435000 ± 3000		
17.47	VLA+PT	AB1134	⋯	423000 ± 5000		
17.19	VLA	15A-310	⋯	395000 ± 13000		
16.59	VLA	15A-310	⋯	371000 ± 14000		
15.49	VLA	15A-310	⋯	329000 ± 5000		
14.99	VLA	15A-310	⋯	308000 ± 7000		
3.598	VLBA(+GBT)	BG221B	2014 Apr 9	18290 ± 310	9110 ± 170	82.2 ± 0.8
1.261	VLBA+GBT	BG221A	2014 Mar 7	2255 ± 61	1243 ± 39	81.9 ± 0.2
0.698	KaVA	r14308a	2014 Nov 4	741 ± 19	434 ± 8	81.2 ± 0.6
0.348	VLBA+LMT	BD183C	2015 Apr 27	215 ± 4	139 ± 4	80.9 ± 3.0
0.131	EHT	2013 Campaign	2013 Mar 21–27	59 ± 6	60 ± 30	

Note. Because of our Monte Carlo error estimation procedure, the size uncertainties are stated relative to the ensemble-average image. They account for thermal noise, systematic noise, limitations of our fitting procedure, and refractive variations of the image size. Note that the errors for each epoch are highly correlated (from all effects apart from thermal noise).

structure. Adding our two estimated uncertainties at quadrature yields our final estimate: $\theta_{\mathrm{maj},0} = 1.380 \pm 0.013$ mas.

We also reanalyzed the VLA observations reported in Bower et al. (2006) using the same procedure as for the VLA observations. These observations included the single VLBA antenna at Pie Town in addition to the VLA, thereby extending the longest baselines by a factor of ≈2. However, they had the disadvantage of a radio transient located only 2″7 south of Sgr A*, with a flux density that was ∼5% of Sgr A* (Bower et al. 2005). For our analysis, we adopted an image-domain approach to remove the transient. Namely, we performed maximum entropy imaging independently for each sub-band. For each image, we then computed the interferometric visibilities for the transient by windowing the image on a region of radius 1″8 centered on the transient. We subtracted these from the measured visibilities (because the Fourier relationship is linear) and used the remainder for Gaussian model fitting to Sgr A*. With this procedure, we found $\theta_{\mathrm{maj},0} = 1.4082 \pm 0.0075$. This value is at modest tension (1.9σ) with the VLA-only results, especially because refractive effects are likely correlated between the two epochs (at these wavelengths, the refractive timescale is ∼100 yr), so each of the two measurements would be similarly biased. Because uncorrected contamination from the transient may bias the measured Gaussian values for Sgr A*, we adopted the measurement and uncertainty of the VLA-only results.

4.2. VLBA Observations at 3.6 cm

We analyzed observations at $\lambda = 3.6$ cm taken with the VLBA in 2014. These observations also included the Green Bank Telescope (GBT), but we did not detect fringes between

the GBT and the inner VLBA, so we only used the inner six VLBA stations (Brewster: BR; Fort Davis: FD; Kitt Peak: KP; Los Alamos: LA; Owens Valley: OV; Pie Town: PT) for our analysis. These observations recorded four contiguous 128 MHz channels and spanned approximately 3.5 hr. They used NRAO 530 as a calibration source. After a global fringe search in AIPS (Greisen 2003), we averaged the data in frequency and in 30 s intervals before Gaussian fitting.

Even without detailed analysis, the effects of refractive substructure are evident in the closure phases of these data. On triangles that resolve the source, the closure phases are markedly non-zero, demonstrating that the underlying image is inconsistent with *any* smooth, scatter-broadened structure (see Figure 2). Our Gaussian fitting procedure gives the major and minor axis sizes to within an estimated uncertainty of less than 2%, even when including refractive effects in the error budget (see Table 1).

After the Gaussian fits, we self-calibrated the full data set to the Gaussian model. However, this procedure must be done with care because the longest baselines are dominated by refractive noise and are inconsistent with the pure Gaussian model. While our approximate prescription for model fitting with substructure (i.e., simply inflating the thermal noise with the rms renormalized refractive noise; see Section 3.2) gives reliable results for Gaussian model fitting, we found that it could downward bias long-baseline visibilities. To perform the self-calibration without biasing long-baseline visibility amplitudes, we first derived time-dependent gain solutions using only "short" baselines, for which the Gaussian model visibility was four times the renormalized refractive noise. We then applied these self-calibration solutions to all baselines. We dropped any visibilities that did not have simultaneous
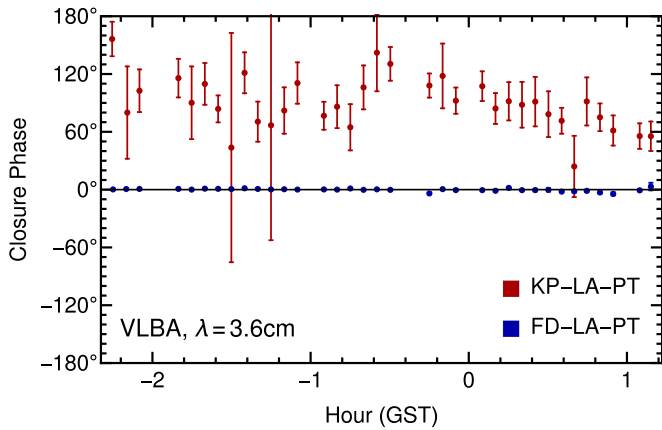
Figure 2. Example closure phases from VLBA observations of Sgr A* at $\lambda = 3.6$ cm. We first computed closure phases on 30 s intervals, then (vector) averaged them in 10 min blocks. We estimated uncertainties via bootstrap resampling within each block. Closure phases on the triangle FD–LA–PT are close to zero, as is expected because these baselines are all dominated by the symmetric Gaussian image rather than substructure (see Figure 3). In contrast, closure phases on the triangle KP–LA–PT are markedly non-zero, demonstrating the clear imprint of refractive substructure breaking symmetry of the smooth ensemble-average image.

self-calibration solutions for both stations. In this way, long baselines that are dominated by refractive noise still obtain reliable self-calibration to the Gaussian model. Figure 3 shows our 3.6 cm data after self-calibration in this way. However, these data only have eight baselines with consistently strong detections (and there are six stations to self-calibrate), so we cannot reliably synthesize an image.

4.3. VLBA Observations at 1.3 cm

We analyzed observations at $\lambda = 1.3$ cm taken with the VLBA+GBT in 2014. These observations were analyzed in Gwinn et al. (2014), who reported the initial discovery of refractive substructure in Sgr A*. As with the 3.6 cm data, these observations recorded four contiguous 128 MHz channels, spanned approximately 3.5 hr, and used NRAO 530 as a calibration source. They include strong detections to the VLBA antennas at North Liberty (NL) and Hancock (HN) in addition to the sites noted in Section 4.2. After a global fringe search in AIPS (Greisen 2003), we averaged the data in frequency and in 30 s intervals before Gaussian fitting. However, we averaged the data to four 128 MHz sub-bands and separately analyzed each.

For these data, the overall baseline coverage is well matched to the scattered image, and we can tightly constrain the Gaussian parameters separately within each sub-band. For each, the thermal uncertainty on the major axis size is less than 0.1%, and we clearly identify the λ^2 scaling of image size across the four sub-bands (see Figure 4). However, the uncertainty from refractive distortion is an order of magnitude larger, so we can only constrain the ensemble-average FWHM to within approximately 1%.

For these data, there is sufficient baseline coverage to reliably synthesize an image. Figure 5 shows a maximum entropy image reconstruction using the EHT-imaging library (Chael et al. 2016). The effects of refractive substructure are evident in the substructure of the image. However, the effects of substructure are most striking in the visibility domain, where

long baselines from GBT to the inner VLBA give strong detections on baselines for which the Gaussian visibility contribution is negligible. Figure 6 shows the final self-calibrated visibilities, following the procedure described in Section 4.2.

4.4. KaVA Observations at 7 mm

The KaVA array has been conducting regular monthly monitoring of Sgr A* at 7 mm since 2014 September as part of the KaVA AGN large program (Kino et al. 2015; Zhao et al. 2017). The KaVA baselines range from 300 to 2300 km and provide excellent (u, v) coverage for Sgr A* observations (Figure 7; see also Akiyama et al. 2014). In particular, the KaVA coverage along the north–south direction is significantly better than VLBA coverage at this frequency, so the KaVA data are better suited to estimate the minor axis size.

We analyzed data from the experiment r14308a, which were obtained in 2014 November. The data were recorded with 256 MHz total bandwidth, spanned 5.5 hr, and had an on-source time for Sgr A* of 220 min. NRAO 530 and two nearby SiO masers (OH 0.55–0.06, VX Sgr) were observed as calibrators (Cho et al. 2017). The correlated data were analyzed with AIPS in a standard pipeline. Most stations had good fringe detections in this experiment. After a global fringe search, the data were averaged in 30 s intervals and across the entire bandwidth for Gaussian model fitting. See G.-Y. Zhao et al. (2018, in preparation) for more details of the monitoring and data analysis.

Figure 7 shows the data from this observation, after our Gaussian model fitting and self-calibration. For these observations, the contribution of renormalized refractive noise is insignificant and is only comparable to the thermal noise on the longest baselines.

4.5. VLBA+LMT Observations at 3.5 mm

For $\lambda = 3.5$ mm, we analyzed data from the first VLBI observations using the Large Millimeter Telescope Alfonso Serrano (LMT) in concert with the VLBA. These observations recorded 480 MHz of bandwidth and spanned 7.5 hr (with approximately 3.4 hr on Sgr A*). We averaged the data in 10 s intervals and across the full bandwidth before Gaussian model fitting. For additional details about these observations, see Ortiz-León et al. (2016), who originally reported and analyzed them.

Using our Gaussian fitting procedure, we found values and uncertainties very close to those reported in Ortiz-León et al. (2016) using self-calibration. This agreement is expected because the only significant adaptation in our current approach is to include refractive noise, and the renormalized refractive noise is less than the thermal noise for all points. More recent data, reported by Brinkerink et al. (2016), also include the GBT and shows marked non-Gaussianity in the closure phases. For these data, which achieve significantly better sensitivity, including refractive noise in the error budget for model fitting may be significant.

4.6. EHT Observations at 1.3 mm

Since 2007, the EHT has observed Sgr A* using a 1.3 mm VLBI array with stations in California, Arizona, and Hawaii. Recently, Lu et al. (2018) reported observations that included a fourth station (in Chile). With only three or four stations, there
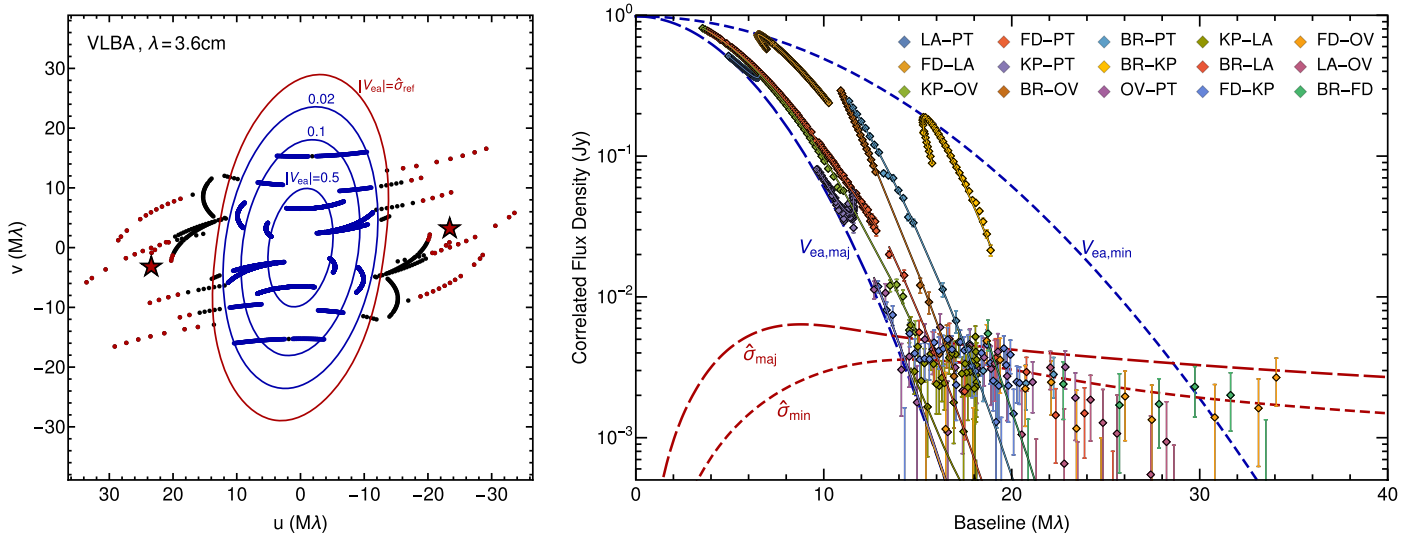
Figure 3. Self-calibrated VLBA data at $\lambda = 3.6$ cm (see Section 4.2). (Left) Final u–v coverage after the cuts described in Section 4.2. Blue points indicate those used for the Gaussian model fits; red points indicate those used to estimate the long-baseline refractive noise, with the red stars denoting their baseline vector average. Blue ellipses show 0.5, 0.1, and 0.02 contour levels of the fitted Gaussian; the red contour shows where the Gaussian visibility is equal to the rms renormalized refractive noise. (Right) Correlated flux density as a function of baseline length. The long/short dashed blue curve shows the best-fit Gaussian visibility function along the major/minor axis. The red curves show the corresponding renormalized refractive noise. Points (with $\pm 1\sigma$ uncertainties) and Gaussian model curves are colored by baseline; baseline labels are ordered by median baseline length. Because of refractive noise, we expect systematic departures at the level of $\hat{\sigma}$ from the Gaussian model curves for each visibility; for a single baseline, these visibilities will be highly correlated over time (see, e.g., the BR-KP and the KP-PT visibilities).
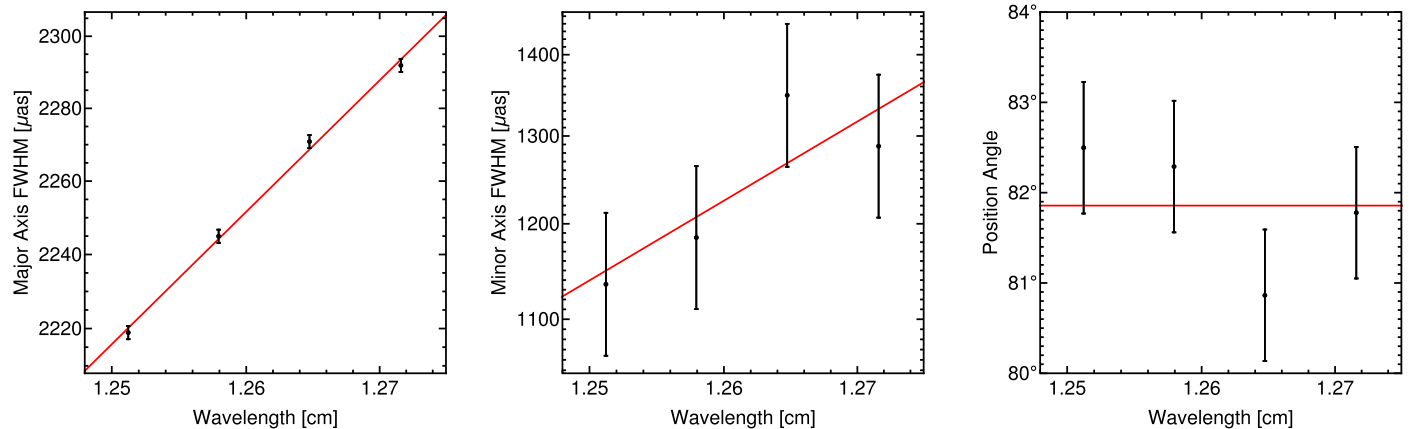
Figure 4. Gaussian parameters for the four sub-bands of the $\lambda = 1.26$ cm observations fitted independently. The scatter among sub-bands when fitting the major axis scattering law is approximately 2 μas, or roughly 0.08% of the image size. However, the uncertainty from refractive fluctuations of the image size (which will give nearly identical bias for each sub-band) is approximately ≈ 20 μas, or 1% of the image size. Thus, the estimated major axis uncertainty relative to the ensemble average size is dominated by refractive image distortion. The close agreement with a λ^2 scaling law (shown in red) strongly suggests that intrinsic structure is heavily subdominant to scatter broadening at this wavelength and also that the inner scale must be larger than the diffractive scale, $r_{\rm in} \gtrsim 300$ km, because otherwise the wavelength dependence of the scattering kernel steepens, $\theta \propto \lambda^{1+\frac{2}{\alpha}}$.

is insufficient baseline coverage to create an image. In addition, the measured visibilities are markedly non-Gaussian (Johnson et al. 2015; Fish et al. 2016; Lu et al. 2018), as expected because of complex intrinsic structure from optically thin emission near the black hole. Nevertheless, even under these circumstances, the image FWHM is still a meaningful quantity that is reliably constrained by sparse coverage because it represents universal behavior of the interferometric visibility function on short baselines (see Section 3.1). Thus, we will now estimate this characteristic FWHM and its uncertainty at 1.3 mm using previously published EHT data.

Because the EHT baseline joining CARMA-SMT (California–Arizona) does not significantly resolve Sgr A* at 1.3 mm, current EHT measurements primarily constrain the

source size in the direction of the California–Hawaii and Arizona–Hawaii baselines, close to east–west (i.e., roughly along the major axis of the scattering kernel). Early detections were consistent with a Gaussian image having a FWHM of approximately 40 μas (Doeleman et al. 2008; Fish et al. 2011). However, more recent measurements with improved sensitivity and calibration find visibility amplitudes on the shortest Hawaii baselines (California–Hawaii) that are strongly inconsistent with the Gaussian model (Johnson et al. 2015; Lu et al. 2018). Thus, the appropriate FWHM is not that of the Gaussian fits, which are incompatible with the data, but can instead be estimated by computing the characteristic FWHM of models that do fit the short- and intermediate-baseline visibility amplitudes.
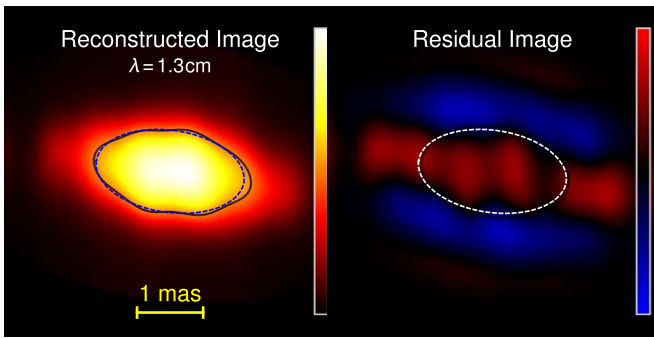
Figure 5. (Left) Reconstructed image at $\lambda = 1.3$ cm. The color scale is linear and ranges from 0–0.33 Jy mas^{-2}. The dashed blue ellipse shows the Gaussian half-maximum contour from model fitting; the solid black line shows the half-maximum contour of the reconstructed image. Substructure is apparent through the subtle distortions from a smooth Gaussian image. (Right) Residual image after subtracting the best-fit Gaussian image. The color scale is linear, and the range extends over ± 0.033 Jy mas^{-2}.

One such model is an annulus. The fitted annulus in Johnson et al. (2015) gives a characteristic FWHM of 58.5 μas for the intrinsic source (as defined in Equation (4)). For comparison, the annulus model from Doeleman et al. (2008) gives 51.5 μas. Two-Gaussian model fits that also include closure phase measurements and baselines to APEX give FWHMs of 55.2 μas and 60.4 μas along the east–west direction or 62.5 μas and 60.5 μas along the major axis of the scattering (for Models A and B of Lu et al. 2018). Because the east–west scatter-broadening is $\lesssim 20$ μas at this frequency, our revisions to the scattering model and remaining uncertainties have little effect on the estimated intrinsic FWHM. The uncertainties are instead dominated by the sparse baseline coverage, and we estimate a plausible range of 51–63 μas for the FWHM of the intrinsic source along the major axis of the scattering based on the span of these fitted models. Note that this range extends beyond the expected diameter of the black hole shadow (51 ± 3 μas), so it does not necessitate that the accretion flow be viewed at large inclination. Accounting for both source and scattering uncertainties, we adopt a plausible range of 53–66 μas for the FWHM of the scattered image of Sgr A* at 1.3 mm along the major axis of the scattering kernel.

The north–south FWHM at 1.3 mm is comparatively poorly constrained. Krichbaum et al. (1998) reported detections of Sgr A* at $\lambda = 1.4$ mm on the baseline joining Pico Veleta and an antenna of the IRAM interferometer at Plateau de Bure. These observations had a baseline length $|\boldsymbol{u}| \approx 0.7 \times 10^9$, but the baseline was aligned close to east–west (position angle approximately 70° east of north). Lu et al. (2018) have recently reported detections at $\lambda = 1.3$ mm on baselines from APEX to California and Arizona, which are oriented close to north–south, but these heavily resolve the source. Thus, they are unreliable for estimating a FWHM using Equation (4) or for computing the second moment of a fitted model. Instead, we estimate a maximum size of the source along the scattering minor axis by requiring that the CARMA-SMT baseline amplitude be at least 80% of the zero-baseline flux density over the Greenwich Sidereal Time (GST) range from -0.5 to 4.0 hr, as is supported by both a priori calibration (Lu et al. 2018) and polarization arguments (Johnson et al. 2015). For a major axis FWHM of ~ 60 μas, this requirement gives an upper limit to the minor axis FWHM of approximately 90 μas. To obtain a corresponding lower limit, we require that the

correlated flux density on the SMT-APEX baselines for the scattered image never exceed 10% of the zero-baseline flux density over the GST range from 0.0 to 2.5 hr (otherwise it would exceed measurements on this baseline; Lu et al. 2018). This constraint only requires that the scattered source have a minor axis FWHM that exceeds 25 μas. Combining these limits, we obtain a plausible range for the FWHM along the scattering minor axis direction of 25–90 μas (of course, the scattering position angle need not correspond to that of the scattered or unscattered image at 1.3 mm).

Finally, we note that the EHT has detected persistent non-zero closure phases of Sgr A* on the California–Arizona–Hawaii triangle, demonstrating that the scattered image structure is not point symmetric (Fish et al. 2016). However, these results do not imply that the intrinsic or scattered FWHM is asymmetric because the non-zero closure phases may be produced by image substructure. For instance, Model B in Lu et al. (2018) fits both the visibility amplitudes and closure phases but has little asymmetry in the FWHM, with major and minor axes FWHMs of 60.5 μas and 60.3 μas, respectively.

5. Composite Constraints on the Scattering and Intrinsic Structure of Sgr A*

We now use our Gaussian model fits and self-calibrated data to constrain the five parameters of our scattering model and estimate the intrinsic structure of Sgr A*. We derive constraints in two stages. First, in Section 5.1, we constrain the three asymptotic Gaussian parameters using our fits to the long-wavelength observations ($\geqslant 1.3$ cm), for which scatter-broadening is dominant over intrinsic structure. Next, in Section 5.2, we jointly constrain α and $r_{\rm in}$ using the observed refractive scattering signatures and limits from the scattering kernel shape and wavelength dependence. With the scattering constraints in place, we show the estimated scattering properties and estimate the intrinsic size of Sgr A* in Section 5.3.

5.1. Constraining the Asymptotic Gaussian Parameters

The three asymptotic parameters of our scattering model can be estimated directly from the Gaussian fits to long-wavelength data. These parameters can also be directly compared with the results of previous studies.

For the major axis normalization, our analysis of the VLA data from 15–30 cm gives $\theta_{\rm maj,0} = 1.380 \pm 0.013$ mas. For comparison, our fits to the 3.6 cm VLBA observation gives $\theta_{\rm maj,0} = 1.412 \pm 0.024$ mas. Thus, the two estimates are consistent to within their stated uncertainties. We will adopt the VLA estimate and uncertainty for our constraint on $\theta_{\rm maj,0}$.

Because we could not reliably fit the minor axis and position angle using the VLA or VLA+PT data, we use VLBI measurements at shorter wavelengths to estimate these parameters. The minor axis of the scattering is small enough at 1.3 cm that intrinsic structure may be significant. Taking only the 3.6 cm measurement and full uncertainty gives $\theta_{\rm min,0} = 0.703 \pm 0.013$ mas. This estimate represents an upper limit to the scattering size because we have not included a contribution from intrinsic structure. However, our representative intrinsic source size derived below using the full set of shorter-wavelength data (see Section 5.3) would bias this upward by only $\lesssim 0.01$ mas, which is within our measurement uncertainty.
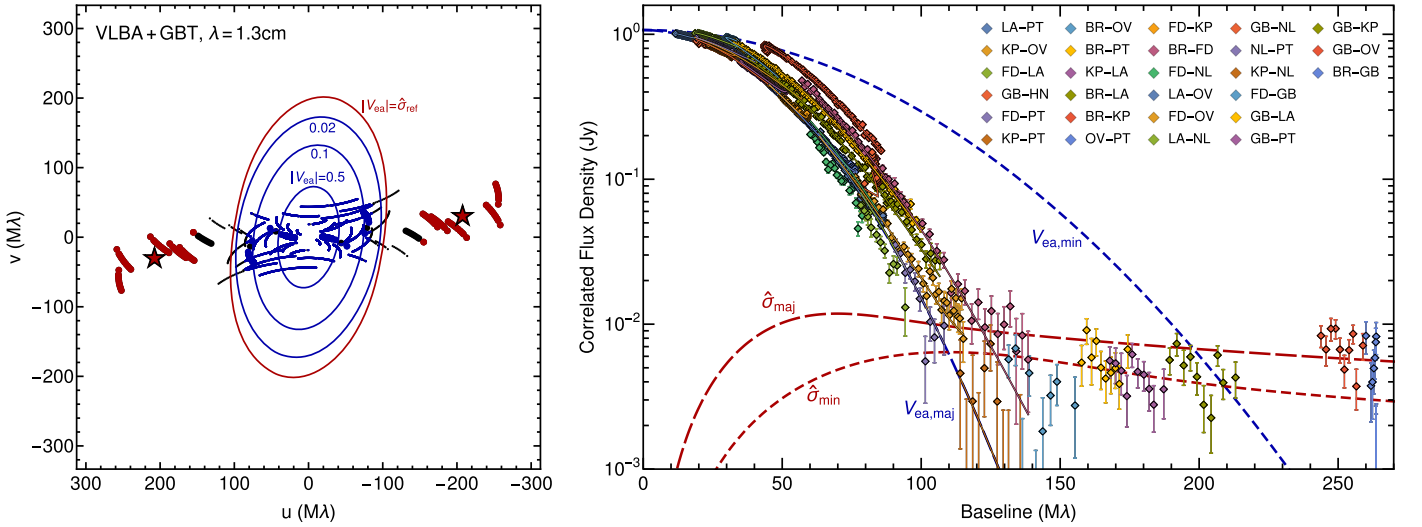
Figure 6. VLBA+GBT observations at $\lambda = 1.3$ cm (see Section 4.3). Panels are as described for Figure 3. Larger points in the left panel denote baselines to the GBT. For clarity, we only show long baselines to GBT on this plot (omitting long baselines to NL and HN, which sample similar (u, v) coordinates but with less sensitivity).
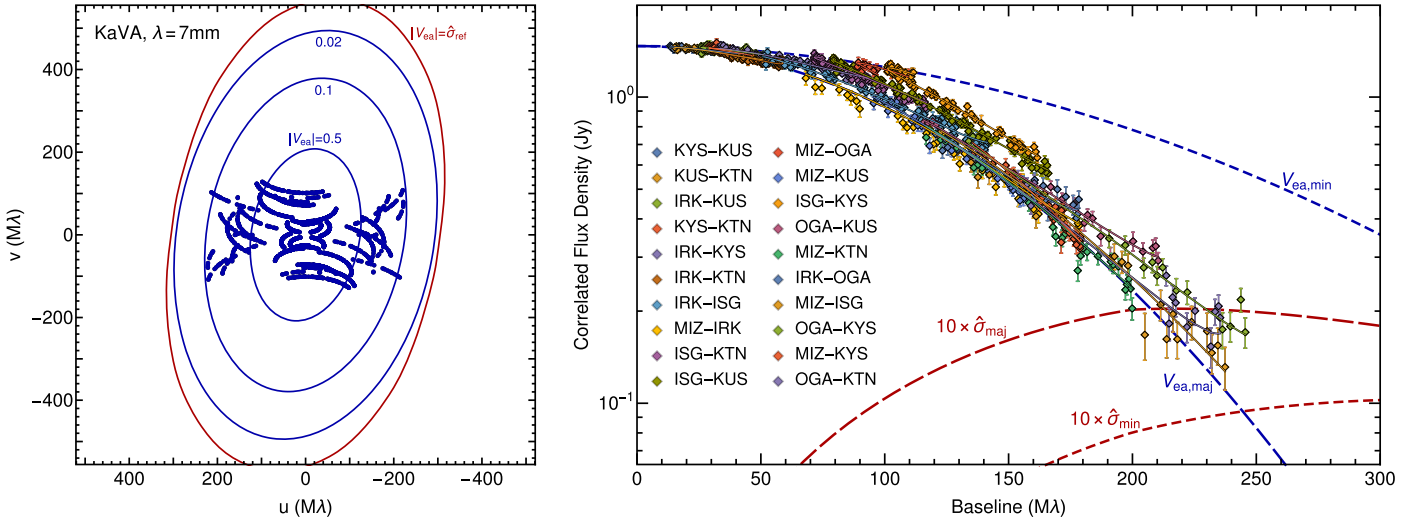

Figure 7. KaVA observations at $\lambda = 0.7$ cm (see Section 4.4). Panels are as described for Figure 3.

Despite the relatively complete baseline coverage at 3.6 cm (see Figure 3), the position angle is rather poorly constrained at this wavelength. The reason for the poor constraint is that there are only eight baselines that are dominated by the Gaussian structure, and these baselines must constrain the (time-dependent) self-calibration solutions for the six participating stations. For comparison, among those same six stations, the 1.3 cm data have fifteen baselines that are dominated by the Gaussian structure. Thus, the self-calibration at 1.3 cm is heavily over-constrained, and the measured position angle has small uncertainties despite the more limited baseline coverage. Because we find a position angle that is consistent with a constant value over wavelengths from 3.5 mm to 3.6 cm, it is unlikely that intrinsic structure changes the position angle appreciably at wavelengths of 1.3 or 3.6 cm. In addition, for the scattering model of Psaltis et al. (2018), the position angle of the scattering kernel is independent of wavelength. Thus, we estimate the scattering position angle by combining the measured position angles at 1.3 cm and 3.6 cm, giving $\phi_{PA} = 81.9 \pm 0.2$.

Table 2
Estimated Asymptotic Gaussian Scattering Parameters

Reference	$\theta_{maj,0}$ (mas)	$\theta_{min,0}$ (mas)	P.A. (deg)
Lo et al. (1998)	1.430 ± 0.020	0.760 ± 0.050	80 ± 3
Shen et al. (2005)	1.390 ± 0.020	0.690 ± 0.060	80
Bower et al. (2006)	1.309 ± 0.015	$0.640^{+0.040}_{-0.050}$	$78^{+0.8}_{-1.0}$
Lu et al. (2011)	1.335 ± 0.014	0.817 ± 0.042	$\cdots$
Psaltis et al. (2015b) [a]	1.320 ± 0.040	0.820 ± 0.210	77.8 ± 9.7
Bower et al. (2015a)	1.320 ± 0.020	0.670 ± 0.020	81.8 ± 0.2
This Work	1.380 ± 0.013	0.703 ± 0.013	81.9 ± 0.2

Notes. These parameters give the scattering kernel at the reference wavelength $\lambda_0 \equiv 1$ cm.
[a] Unlike the other entries in this table, Psaltis et al. (2015b) reanalyzed a sample of published Gaussian parameter fits rather than analyzing new or archival observations directly.

Table 2 compares our newly derived Gaussian parameters with previously reported estimates. Note that the three observations used to derive our parameter estimates (2015
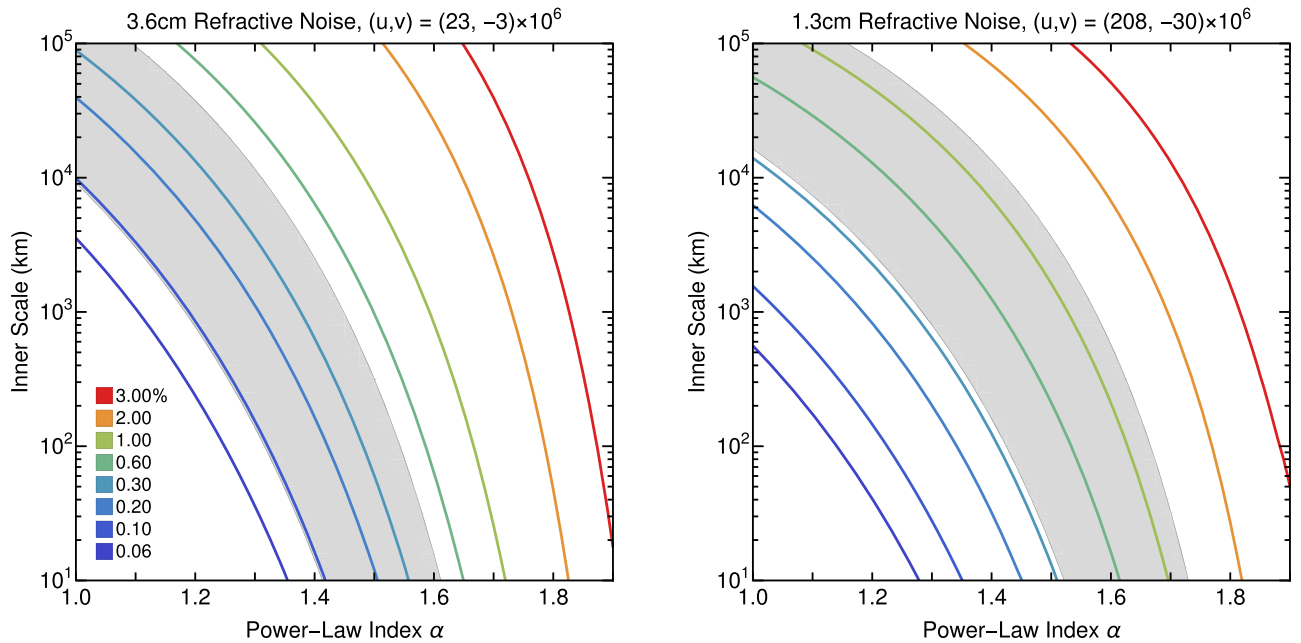
Figure 8. (Left) Expected amplitude of the renormalized refractive noise $\hat{\sigma}_{\rm ref}$ at $\lambda = 3.6$ cm on the baseline $(u, v) = (23.4, -3.2) \times 10^6$ as a function of α and $r_{\rm in}$. Colored contours show predicted values of $\hat{\sigma}_{\rm ref}$; the gray shaded region shows the 95% confidence range determined by the measured refractive noise (see Section 5.2.1). For the model values, we approximate the ensemble-average image size at each wavelength using our measured size. Thus, the assumed intrinsic size depends on α and $r_{\rm in}$ because the scattering kernel depends on them. (Right) Amplitude of the refractive noise at $\lambda = 1.3$ cm on the baseline $(u, v) = (207.6, -30.4) \times 10^6$ as a function of α and $r_{\rm in}$. The gray shaded region shows the 95% confidence range determined by the measured refractive noise.

VLA observations, and VLBA observations at 3.6 and 1.3 cm) were not used by any of these previous studies. Relative to past work, the major and minor axes are consistent with the values found by Shen et al. (2005), but our major axis normalization is 4.7σ larger than the estimate of Bower et al. (2006) and 3σ larger than that of Bower et al. (2015a) (both relied on the same VLA+PT image-domain analysis at long wavelengths). Our major axis uncertainty is similar to these previous results, largely because of the increased error budget to accommodate refractive fluctuations, while our minor axis uncertainty is significantly smaller than all past work. While our position angle is somewhat larger than most previous studies, it is close to the value and uncertainty estimated by Bower et al. (2015a).

5.2. Constraining α and $r_{\rm in}$

The remaining two parameters of our scattering model, α and $r_{\rm in}$, can be constrained in two ways: through a change in the scatter-broadening law from its asymptotic behavior at long wavelengths and through stochastic signatures of refractive scattering. For both types of constraints, the effects of α and $r_{\rm in}$ must be considered jointly; α will determine the asymptotic behavior at short wavelengths, but $r_{\rm in}$ determines the scale on which the scattering transitions between the two asymptotic regimes. Many previous efforts have constrained α by fitting the wavelength dependence of scatter-broadening to a power law λ^β or by quantifying Gaussianity of the scattered image (e.g., Lo et al. 1998; Bower et al. 2004; Lu et al. 2011). However, these studies have implicitly assumed the limit $r_{\rm in} \to 0$, effectively fitting centimeter data to the properties of the scattering expected for the asymptotic regime $\lambda \to 0$. As we will demonstrate, jointly fitting the two parameters is imperative to derive meaningful parameter constraints for α and $r_{\rm in}$.

We will now derive a series of constraints α and $r_{\rm in}$. In Section 5.2.1, we derive constraints from the refractive noise

on long baselines at 3.6 and 1.3 cm. In Section 5.2.2, we determine constraints from the stringent limits on refractive fluctuations of the image size at 7 mm. In Section 5.2.3, we derive constraints based on the λ^2 scaling of scatter broadening at centimeter wavelengths. In Section 5.2.4, we establish constraints based on Gaussianity of the scattered image at 1.3 cm. While any of these individual constraints can only weakly constrain the parameter pair $(\alpha, r_{\rm in})$, the cumulative constraints are quite restrictive, summarized in Figure 9. We discuss these constraints and give our recommended characteristic values in Section 5.2.5.

5.2.1. Constraints from Refractive Noise at 3.6 and 1.3 cm

For a single long-baseline visibility measurement, the refractive noise is drawn from a circular Gaussian distribution. On baselines that heavily resolve the ensemble-average image, the visibility amplitude is then drawn from a Rayleigh distribution. However, the mean of this distribution is poorly constrained by a single measurement. Moreover, refractive noise among nearby baselines will be correlated, with a correlation length that is comparable to the length of baselines that begin to resolve the source (Johnson & Narayan 2016). Consequently, our long baselines at 3.6 and 1.3 cm only sample a few independent realizations of the refractive noise.

To combine measurements from multiple baselines, we adopted a simple procedure. First, we only examined visibilities that were reliably dominated by refractive noise, with negligible contribution from the ensemble-average structure. At 3.6 cm, we used the cut $20 \times 10^6 < |\boldsymbol{u}| < 40 \times 10^6$, while at 1.3 cm we used $150 \times 10^6 < |\boldsymbol{u}| < 300 \times 10^6$. Next, we performed an unweighted scalar average of the noise-debiased visibilities on these baselines. We used this average as an approximation to the mean renormalized refractive noise on the vector average of the baselines, for
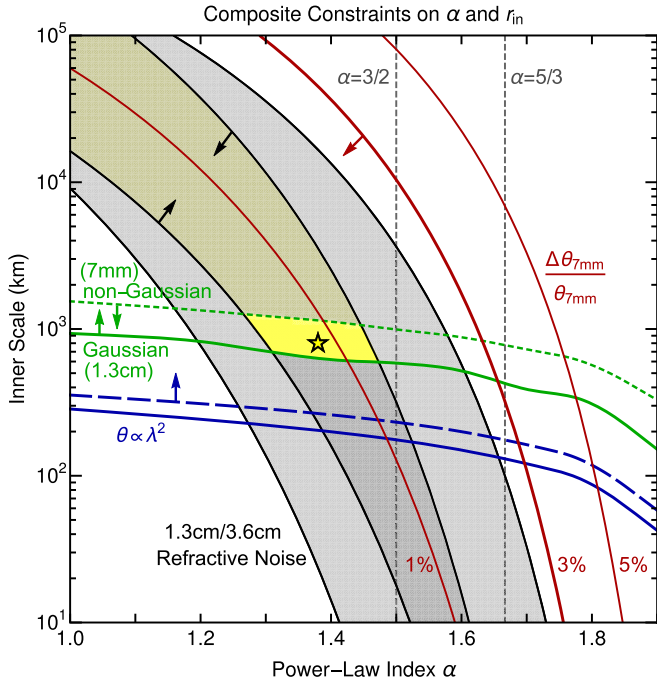
Figure 9. Composite constraints on α and r_{in}. Blue lines show α-dependent *lower* limits on r_{in} from the λ^2 scaling of image size (major axis: solid, minor axis: dashed; see Section 5.2.3). The solid green line shows the *lower* limit on r_{in} from the measured Gaussian image shape at 1.3 cm, while the dotted green line shows the (more tentative) *upper* limit on r_{in} from the measured non-Gaussian image shape at 7 mm (see Section 5.2.4). Red lines show contours of 1%, 3%, and 5% for rms fluctuations of the major axis size at $\lambda = 7$ mm; these fluctuations are constrained to be less than 3%, giving an α-dependent *upper* limit on r_{in} (see Section 5.2.2). Combining these constraints, the yellow shaded region shows the plausible range of α and r_{in}; the darker yellow region shows the range without including the non-Gaussian measurement at 7 mm. Overall, we find that $\alpha \lesssim 1.47$ and $r_{in} \gtrsim 600$ km. The star marks our recommended characteristic values: $\alpha = 1.38$ and $r_{in} = 800$ km (see Section 5.2.5).

which we expect $\langle |V(\boldsymbol{b})| \rangle = \frac{\sqrt{\pi}}{2}\hat{\sigma}_{ref}(\boldsymbol{b}) \approx 0.89\hat{\sigma}_{ref}(\boldsymbol{b})$. The average baseline was $(u, v) = (23.4, -3.2) \times 10^6$ at 3.6 cm and $(u, v) = (207.6, -30.4) \times 10^6$ at 1.3 cm.

In this way, we obtained an estimate of $\hat{\sigma}_{ref}$ on a single baseline at each wavelength. This simplification facilitates direct comparisons with predictions for $\hat{\sigma}_{ref}$ from a scattering model. To validate this reduction and determine a confidence interval for our refractive noise estimates, we generated 1000 simulated images of the scattering at both wavelengths. For each image, we calculated the visibilities on all the long baselines for the 3.6 and 1.3 cm observations and computed the scalar average of the visibility amplitudes. At 3.6 cm, the mean amplitude of the sampled refractive noise (averaged over all the long baselines and the multiple simulations) was within 10% of the mean amplitude for refractive noise of the average baseline. For averaged visibility amplitudes for individual image realizations, 95% of values fell between 0.40 and 1.90 times the expected mean value for the fixed baseline. For draws of a Rayleigh distributed random variable, the middle 95% of samples will extend to 0.18 and 2.2 times the mean. Thus, our simple averaging scheme significantly tightens the bounds on $\hat{\sigma}_{ref}$ by combining multiple correlated measurements. At 1.3 cm, the mean amplitude of the refractive noise averaged over long baselines was within 0.1% of the mean value on the average baseline. The middle 95% of samples fell within the range of 0.45 to 1.70 times the expected mean noise amplitude on the fixed baseline.

With this approach, we thereby estimate 95% confidence intervals for σ_{ref} of [0.096%, 0.45%] at $(u, v) = (23.4, -3.2) \times 10^6$ for 3.6 cm, and [0.32%, 1.2%] at $(u, v) = (207.6, -30.4) \times 10^6$ for 1.3 cm (both are expressed as a fraction of the total flux density). Figure 8 shows the expected values for σ_{ref} at both wavelengths as a function of α and r_{in}; the gray shaded regions show the 95% confidence intervals for α and r_{in} based on the refractive noise measurements at both wavelengths.

5.2.2. Constraints from Refractive Fluctuations of the Image Size

Refractive scattering causes variations in the observed angular size of a source (Blandford & Narayan 1985). For observations that span many refractive timescales, the observed level of variability can then be used to constrain the scattering model. Because the intrinsic source may also be time-variable, measurements of the image size variability can only give an upper limit for the variations attributable to scattering. As with other refractive effects, fluctuations of image size will increase with increasing α and r_{in}.

For Sgr A*, the most stringent constraints on image size fluctuations come from observations at $\lambda = 7$ mm. Even without accounting for refractive noise, observations over the past 25 years or so consistently find a major axis size in the range of 680–750 μas (e.g., Backer et al. 1993; Krichbaum et al. 1993; Lo et al. 1998; Bower et al. 2004, 2014b, 2015a; Lu et al. 2011; Akiyama et al. 2014; Zhao et al. 2017). A uniform distribution over the entire range 680–750 μas has a standard deviation of 20.2 μas, or fractional variations of 2.8%. Note that this range is inflated by measurement uncertainties in the reported sizes (in addition to scattering and intrinsic variability). Thus, we estimate that the fractional scatter of the major axis size at $\lambda = 7$ mm from refractive distortion is certainly less than 3%.

We can compare this limit to the expected refractive fluctuations, which can be computed semi-analytically via the framework for renormalized refractive noise developed in Appendix A. Namely, on short baselines, the renormalized refractive noise is dominated by refractive fluctuations in image size. For a short baseline $\boldsymbol{u}$, the renormalized visibility (i.e., the visibility after normalizing the total flux density and centering the image) is given by

$$\hat{V}(\boldsymbol{u}) = 1 - \frac{\pi^2}{4\ln 2}\theta_\parallel^2 u^2 + \mathcal{O}(\theta_\parallel^3 u^3), \qquad (5)$$

where $\theta_\parallel$ is the source size projected along the baseline direction (see Equations (3) and (4)). Because of scattering, the instantaneous source size will not match the ensemble-average value, $\langle \theta_\parallel \rangle$; this discrepancy is what produces renormalized refractive noise $\hat{\sigma}_{ref}(\boldsymbol{u})$ on short baselines. Explicitly,

$$\hat{\sigma}_{ref}(\boldsymbol{u}) = \sqrt{\langle \Delta \hat{V}(\boldsymbol{u})^2 \rangle}$$
$$\approx \frac{\pi^2}{4\ln 2}u^2\sqrt{\langle(\theta_\parallel^2 - \langle\theta_\parallel\rangle^2)^2\rangle}$$
$$\approx \frac{\pi^2}{2\ln 2}u^2\langle\theta_\parallel\rangle\sqrt{\langle\Delta\theta_\parallel^2\rangle}$$

$$\Rightarrow \frac{\sqrt{\langle\Delta\theta_\parallel^2\rangle}}{\langle\theta_\parallel\rangle} \approx \frac{2\ln 2}{\pi^2}\frac{\hat{\sigma}_{ref}(\boldsymbol{u})}{u^2\langle\theta_\parallel\rangle^2}. \qquad (6)$$

The red lines in the right panel of Figure 9 show contours for the values of α and r_{in} that would produce 1%, 3%, and 5%

fractional fluctuations of the major axis size at $\lambda = 7$ mm. For these calculations, we hold the ensemble-average image size fixed (approximating it by our measured size), so the intrinsic size is also a function of these parameters because the scattering kernel depends on them. The requirement that the fluctuations are smaller than 3% then gives an α-dependent upper-limit on r_{in}.

Observe that the shapes of the image fluctuation contours are very similar to those of the refractive noise at 1.3 cm on the fixed baseline $\boldsymbol{u} = (207.6, -30.4) \times 10^6$. This similarity is expected because both effects are dominated by scattering modes on the same angular scale. Specifically, at 7 mm, the dominant modes for image distortion are on the scale of the image size, $\theta_{maj} \approx 0.7$ mas. At 1.3 cm, the dominant modes for refractive noise are those matched to the angular resolution of the long baselines, $1/|\boldsymbol{u}| \sim 1$ mas.

5.2.3. Constraints from the λ^2 Scaling of Scattered Size

The constant scaling of image size as $\theta \propto \lambda^2$, stable image anisotropy, and constant position angle at wavelengths $\lambda \gtrsim 1.3$ cm strongly argue against a departure of the angular broadening from the asymptotic λ^2 law in this interval, as that would require intrinsic structure to fortuitously offset the change in angular broadening. Likewise, these properties argue against intrinsic structure being significant at these wavelengths. This plausibility argument gives a lower bound on the inner scale because the angular broadening asymptotes to $\theta \propto \lambda^{1+\frac{2}{\alpha}}$ as $\lambda \to 0$, with the transition when the diffractive scale becomes larger than the inner scale.

The diffractive scale is larger at shorter wavelengths, so our most stringent constraints on r_{in} come from the shortest wavelengths that exhibit the λ^2 law. We have found close agreement with the λ^2 law across the observing bandwidth at 1.3 cm (see Figure 4), so the inner scale must exceed the diffractive scale at 1.3 cm: $r_{in} \gtrsim 300$ km. The limit is slightly higher for lower values of α because they asymptotically give a stronger departure from λ^2 scaling. The limit is slightly higher for the minor axis than for the major axis because the former has a larger diffractive scale.

Blue lines in the right panel of Figure 9 show α-dependent lower limits on r_{in} using the simple condition that the $\lambda = 1.3$ cm angular broadening cannot be more than 5% smaller than the value extrapolated from $\lambda \to \infty$ with a pure λ^2 scaling (i.e., the limit as $r_{in} \to \infty$). Requiring that the scaling across the full $\lambda = 1.3$ cm bandwidth match a λ^2 law to within the uncertainties shown in Figure 4 gives a similar constraint.

5.2.4. Constraints from the Image Gaussianity

We can also constrain α and r_{in} from the shape of the scatter-broadened image at a fixed wavelength. At long wavelengths, the scatter-broadening is Gaussian and the visibility function falls as e^{-u^2}, while at short wavelengths the visibility function falls as e^{-u^α}. As in Section 5.2.3, this constraint is really a plausibility argument; the intrinsic source could fortuitously offset any change in the angular broadening function to produce a Gaussian image despite non-Gaussian scattering, and non-Gaussian source structure could mimic the behavior of a non-Gaussian scattering kernel. Thus, we focus these tests on our 1.3 cm and 7 mm observations, where the baseline coverage is excellent and source structure is subdominant to scatter broadening.

Once again, the transition between the two scaling regimes depends on the inner scale. Specifically, the scattering kernel will depart from a Gaussian for baselines with physical lengths $b \gtrsim (1 + M)r_{in}$, where $M \approx 0.53$ for Sgr A* (see Section 2.3). At 1.3 cm, the longest baselines that are not dominated by refractive noise are ~ 100 M$\lambda \approx 1300$ km, so these observations can, in principle, constrain r_{in} to be greater than ~ 800 km. The lower limit is expected to increase with decreasing α because of a sharper deviation from the Gaussian kernel with decreasing α.

To derive constraints on α and r_{in} using image Gaussianity tests, we fit our 1.3 cm and 7 mm observations with the full, non-Gaussian kernel of our scattering model. For each case, we included refractive noise in the error budget as we did for Gaussian fits. For the 1.3 cm fits, we used a point-source model for the intrinsic structure. This procedure then quantifies the baseline length at which visibilities become inconsistent with a Gaussian curve; this break is insensitive to the distinction between intrinsic structure and scattering because of the convolution action of scattering in the visibility domain. We found the best fits to the 1.3 cm data were those with $r_{in} \to \infty$ (giving a perfectly Gaussian image). Thus, the fits give an α-dependent *lower* limit for r_{in}. The solid green curve shown in Figure 9 corresponds to the values with an increase of 4 in the total chi-squared of the fitted model, corresponding to a 2σ confidence contour. These limits range from $r_{in} \gtrsim 520$ km for $\alpha = 1.6$ to $r_{in} \gtrsim 930$ km for $\alpha = 1.0$, in line with expectations from the simple calculation in the previous paragraph.

For the 7 mm data, intrinsic structure is non-negligible, so we fixed the Gaussian scattering parameters to the estimates from Section 5.1 and then fit for the three parameters of an anisotropic intrinsic Gaussian source along with α and r_{in}. These fits show a strong indication of non-Gaussian structure, with an increase in total chi-squared for a purely Gaussian model of 19.2 relative to the best-fitting models with a finite inner scale (i.e., a $\gtrsim 4\sigma$ preference for a non-Gaussian image). The fits then provide an α-dependent *upper* limit for r_{in}. This test must be interpreted with caution, as the intrinsic source structure is non-negligible at this wavelength and may be non-Gaussian, although it is expected to be Gaussian on baselines that do not significantly resolve the intrinsic source (see Section 3.1). Because the KaVA baselines only modestly resolve the scattered source, this assumption is likely acceptable. Nevertheless, we still use a slightly higher threshold for these results relative to those at 1.3 cm because the plausibility argument is weaker. Thus, the dotted green curve shown in Figure 9 corresponds to the values with an increase of 9 in the total chi-squared of the fitted model relative to the best-fit model, corresponding to a 3σ confidence contour. However, when the residual gain priors on the a priori calibration are unconstrained, the significance of the finite inner scale is only $\approx 1\sigma$. Thus, we regard this detection of visibility amplitude non-Gaussianity and the corresponding upper limit on r_{in} as tentative.

5.2.5. Recommended Characteristic Values for α and r_{in}

For our recommended characteristic value for the inner scale, we adopt $r_{in} = 800 \pm 200$ km, based on the combined image Gaussianity tests at 1.3 cm and 7 mm and the refractive noise constraints for 3.6 and 1.3 cm. However, while the lower limit at ~ 600 km is relatively firm, we regard the upper limit as somewhat tentative without confirmation from additional 7 mm observations and from tests at other wavelengths.

Table 3
Estimated Scattering Model for Sgr A*

Parameter	Estimate
Geometrical parameters	
Scattering screen magnification	$M = D/R = 0.53 \pm 0.08$
Earth-scattering distance	$D = 2.7 \pm 0.3$ kpc
Sgr A*-scattering distance	$R = 5.4 \pm 0.3$ kpc
Scattering parameters	
Reference wavelength	$\lambda_0 \equiv 1$ cm
Gaussian major axis FWHM	$\theta_{\text{maj},0} = 1.380 \pm 0.013$ mas
Gaussian minor axis FWHM	$\theta_{\text{min},0} = 0.703 \pm 0.013$ mas
Gaussian position angle	$\phi_{\text{PA}} = 81°9 \pm 0°2$
Power-law index of $D_\phi(\boldsymbol{r})$	$\alpha = 1.38^{+0.08}_{-0.04}$
Power-law index of $Q(\boldsymbol{q})$ and $P_{n_e}(\boldsymbol{q})$	$\beta = \alpha + 2 = 3.38^{+0.08}_{-0.04}$
Inner scale	$r_{\text{in}} = 800 \pm 200$ km
Scattering transitions	
Gaussian–inertial kernel transition	$\lambda = 5$ mm
Weak–strong scattering transition	$\lambda = 0.2$ mm

Note. Values and uncertainties for α, β, and r_{in} use our tentative upper-limit from non-Gaussianity at 7 mm (see Figure 9). We define the Gaussian-inertial kernel transition as the wavelength for which the diffractive scale and inner scale are equal. At significantly longer wavelengths, the scattering kernel will be Gaussian (determined by the three asymptotic Gaussian parameters); at significantly shorter wavelengths, the shape will be determined by α. The weak–strong transition is the wavelength for which the diffractive scale and refractive scale are equal. For Kolmogorov turbulence, $\alpha = 5/3$ and $\beta = 11/3$.

To obtain a characteristic value for α, we then use the joint likelihood function of the 1.3 and 3.6 cm refractive noise with r_{in} as estimated above. As in Section 5.2.1, we used 1000 scattering realizations at both wavelengths. For each realization, we sampled and then averaged visibilities on the long baselines, following our procedure for the data. This sample then provides an estimate for the likelihood function for $\hat{\sigma}$ on the characteristic baseline at each wavelength. The joint likelihood function then gives $\alpha = 1.38^{+0.08}_{-0.04}$, where $\alpha = 1.38$ is the maximum likelihood estimate.

5.3. The Scattering Kernel and Intrinsic Structure of Sgr A*

Using the scattering model determined in Sections 5.1 and 5.2, we now explore the expected scattering properties for Sgr A* and estimate its wavelength-dependent intrinsic size. Table 3 summarizes our estimates for the parameters of this scattering model and provides additional derived quantities.

Figures 10 and 11 show our estimated major axis FWHM, minor axis FWHM, and position angle as a function of wavelength (these values are given in Table 1). After normalizing by λ^{-2}, these sizes show a significant increase with decreasing wavelength for $\lambda \lesssim 1.3$ cm. Because $\alpha < 2$, the scattering law can only become steeper than λ^2 at short wavelengths. Thus, this increase in normalized size robustly indicates intrinsic structure at millimeter wavelengths.

Figures 10 and 11 also show the estimated FWHM of the scattering kernel, including the uncertainty spanned by the plausible range of α and r_{in} (see Figure 9). For these estimates, we do not define the FWHM using the second derivative of the visibility amplitude on a zero baseline (as in Section 3.1). We instead identify the baseline length at which the scattering kernel falls to half, $\exp\left[-\frac{1}{2}D_\phi(\boldsymbol{u}_{1/2}/(1 + M))\right] \equiv 1/2$, and then derive a representative image FWHM based on the

relationship for a Gaussian image: $\theta_{\text{FWHM}} = \frac{2\ln 2}{\pi u_{1/2}}$. The kernel uncertainties become larger at shorter wavelengths because of our limited constraints on α and r_{in}. At 1.3 mm, the uncertainty is $\sim$20% on both the major and minor axis FWHM.

Figure 12 shows our estimates of the visibility domain scattering kernel and its uncertainties at six representative wavelengths. This kernel is required to "deblur" measurements of Sgr A*, so it is fundamental to scattering mitigation strategies (Fish et al. 2014; Johnson 2016). At millimeter wavelengths, the kernel differs significantly from the prediction of the simple Gaussian/λ^2 model, and the remaining uncertainty in the scattering kernel on long baselines is significant, primarily because of uncertainties on α and r_{in}. Thus, we expect that the blurring effects of scattering are significantly weaker than have been assumed for Sgr A*.

With the estimated size of the scattering kernel in place, we can deconvolve the scattering from the observed Gaussian size to estimate an intrinsic FWHM at each wavelength. Table 4 and Figure 13 show the estimated intrinsic size along the major and minor axes of the scattering kernel as a function of wavelength. The plotted uncertainties account for uncertainties in our estimates of the scattered size (from thermal noise, systematic effects, and refractive distortion) and in the estimated scattering kernel. The inferred intrinsic size is nearly isotropic and scales approximately as $\theta \propto \lambda$. The largest intrinsic anisotropies are at 3.5 mm (up to $\sim$1.3:1) and 1.3 mm (up to $\sim$2:1, but poorly constrained). Because the total flux density I_0 of Sgr A* rises with frequency over this range (see, e.g., Lu et al. 2011; Bower et al. 2015b), the brightness temperature $T_b \propto \lambda^2 \theta_{\text{src}}^{-2} I_0$ also rises. For instance, using $\theta_{\text{src}} \sim (40\ \mu\text{as}) \times \lambda_{\text{mm}}$, we estimate $T_b \sim 1.1 \times 10^{10}$ K at 1.3 cm and $T_b \sim 3.1 \times 10^{10}$ K at 1.3 mm.

6. Discussion

6.1. The Intrinsic Structure of Sgr A*

Our estimates for the approximately linear wavelength dependence of intrinsic size are typical for stratified emission in synchrotron self-absorbed systems (e.g., Blandford & Königl 1979; Falcke & Markoff 2000; Davelaar et al. 2018), and they are plausible for both disk- and jet-dominated models for the radio emission of Sgr A*. However, the lack of asymmetry in the inferred intrinsic size and the stable position angle of the scattered image both argue against intrinsic structure that is highly asymmetric for 3.5 mm $\lesssim \lambda \lesssim$ 1.3 cm. For instance, the model of Falcke & Markoff (2000) predicts an image asymmetry of roughly 4:1, and recent general relativistic magnetohydrodynamic (GRMHD) simulations of jets show asymmetry of $\sim$2:1 at 7 mm (Davelaar et al. 2018). The intrinsic size of Sgr A* we find is qualitatively consistent with radiatively inefficient accretion flow (RIAF) models (e.g., Özel et al. 2000; Yuan et al. 2003; Yuan & Narayan 2014), which are more plausible for producing a nearly isotropic image at wavelengths as long as 1.3 cm. Recent general relativistic radiation magnetohydrodynamic (GRRMHD) simulations show good agreement with our estimated size at 1.3 mm and also show a similar size trend, but they generally underpredict the size at 7 mm and 1.3 cm (Chael et al. 2018), perhaps highlighting the contribution from a non-thermal population of electrons.

Note that there has not been consistency in how image FWHM from simulations is defined. For comparison with Gaussian image sizes reported here and elsewhere, simulations should compute the image FWHM from the second moment along principal axes of the image brightness distribution (see Section 3.1). While some simulation papers have adopted this
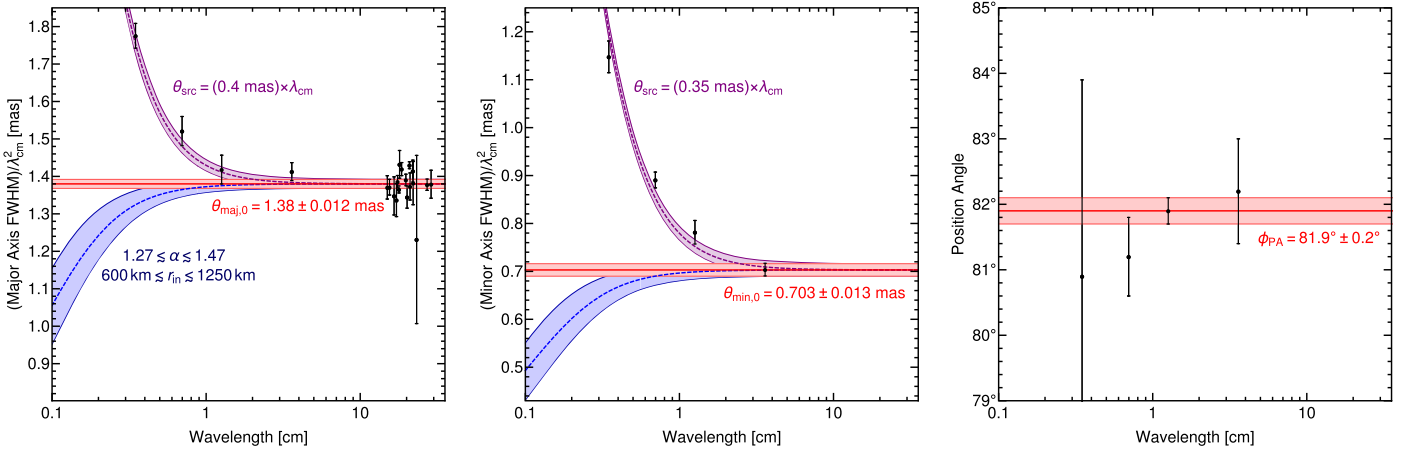
Figure 10. Gaussian parameters of the scattered image of Sgr A* as a function of wavelength. Major and minor axes sizes are normalized by λ^{-2}. Black points show our measurements with $\pm 1\sigma$ uncertainties (Table 1). The red region shows our fitted asymptotic parameters $\theta_{maj,0}$, $\theta_{min,0}$, and ϕ_{PA} with their respective uncertainties. The blue region shows the plausible range of values for the scattering kernel based on our constraints on all scattering parameters, including α and r_{in} (see Figure 9). The purple region shows the size corresponding to a simple source model, with $\theta_{src} \propto \lambda$, added at quadrature to the scattering law, with the associated scattering model uncertainty. The blue and purple dashed curves show the results corresponding to our recommended characteristic values for α and r_{in}.
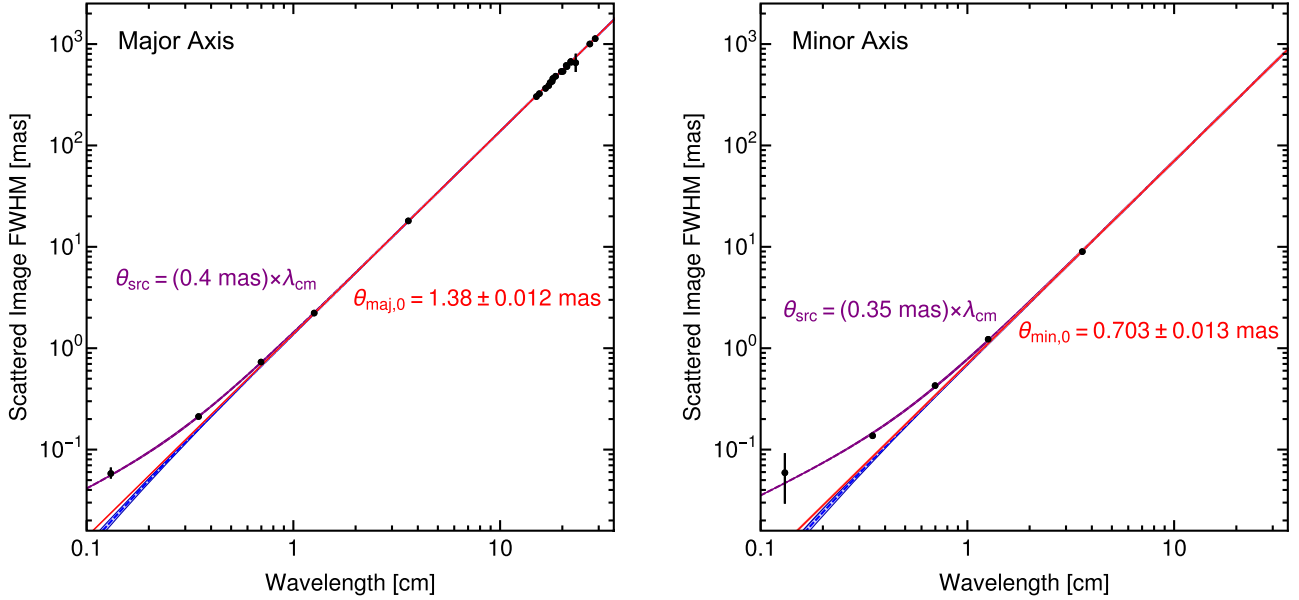
Figure 11. Same as Figure 10, but without normalizing sizes by λ^{-2}.

convention for comparison (e.g., Mościbrodzka et al. 2009, 2012; Chael et al. 2018; Davelaar et al. 2018), others have developed ad hoc definitions for the reported image size (e.g., Falcke & Markoff 2000; Özel et al. 2000; Chan et al. 2015; Psaltis et al. 2015a) or do not state their procedure for estimating the size. An alternative is to fit or compare simulations directly to measured interferometric visibilities (e.g., Broderick et al. 2009, 2016; Dexter et al. 2010; Kim et al. 2016; Pu et al. 2016; Gold et al. 2017).

6.2. Implications for Interstellar Scattering

We now re-evaluate our assumptions for the scattering of Sgr A*, and discuss implications of our findings.

6.2.1. The Outer Scale of Turbulence

All of our calculations and model fits have assumed that the outer scale of turbulence is effectively infinite. We now

evaluate this assumption a posteriori. In particular, Goldreich & Sridhar (2006) estimated that $r_{out} \lesssim 10^{11}$ cm $\times \left(\frac{R}{130\,\text{pc}} \right)^{5/2} \times \left(\frac{T}{10^4\,\text{K}} \right)^{3/4}$. For the previously assumed value of $R = 130$ pc (Lazio & Cordes 1998), they noted that this scale is unacceptably small, as it produces too much heating and it does not correspond to a reasonable astronomical scale for nonlinear density fluctuations. In addition to these objections, our measurements of refractive noise give a lower bound for the outer scale because refractive noise will be suppressed on angular scales larger than $\sim r_{out}/D$. Thus, our measurements of refractive noise on baselines with $|\mathbf{u}| \sim 10^7$ at 3.6 cm show that $r_{out} \gtrsim (2\pi)^{-1} D/10^7 \sim 10^{14}$ cm. With the modified distance to the scattering (see Section 2.3 and Bower et al. 2014a), the problems identified by Goldreich & Sridhar (2006) are mitigated, as we now discuss in detail.

Specifically, an upper limit on the outer scale can be estimated as the scale on which the scattering power spectrum
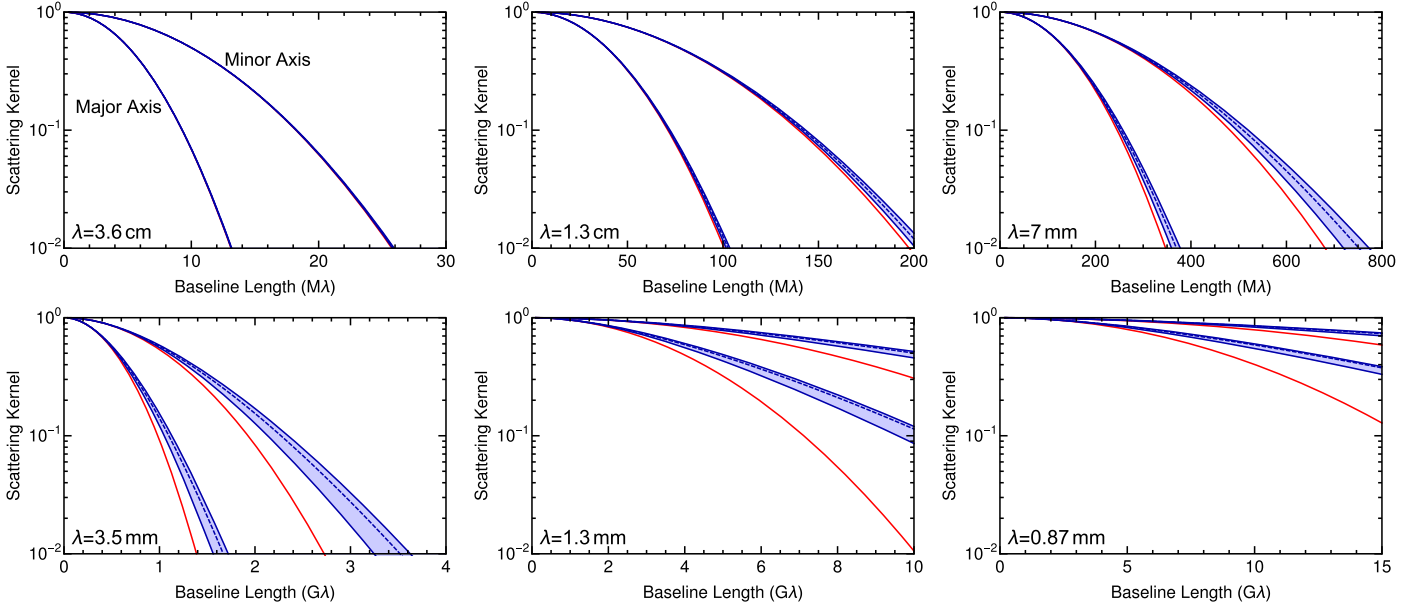
Figure 12. Scattering kernel of Sgr A* as a function of baseline length along the major and minor axes at representative wavelengths. For each panel, the red curves correspond to a Gaussian kernel with our measured scattering parameters, the blue shaded region shows the plausible range of values based on our constraints on the scattering model, and the dashed blue line shows the kernel corresponding to our recommended characteristic values for the scattering parameters. For baselines much longer than the inner scale, the kernel is non-Gaussian, falling as $e^{-b^{\alpha}}$ rather than $e^{-b^{2}}$. For the EHT, which has baselines extending to $\sim$6 Gλ along the major axis and to $\sim$9 Gλ along the minor axis at 1.3 mm, the expected kernel differs significantly from the Gaussian prediction, and we expect that the effects of scattering are substantially weaker than have been assumed. Because of its intrinsic structure, Sgr A* is heavily resolved for baselines of 3–6 Gλ (e.g., Lu et al. 2018); the remaining kernel uncertainties may have minimal effects for imaging at 1.3 and 0.87 mm (see, e.g., Figure 11).

Table 4
Estimated Intrinsic Size of Sgr A*

λ (cm)	θ_{maj} (μas)		θ_{min} (μas)	
	Char.	Plausible	Char.	Plausible
3.598	4000^{+1200}_{-1900}	4000^{+1800}_{-4000}	...	...
1.261	550^{+210}_{-370}	550^{+280}_{-550}	560^{+80}_{-90}	560^{+120}_{-160}
0.698	327^{+41}_{-46}	327^{+58}_{-69}	274^{+12}_{-13}	274^{+23}_{-25}
0.348	143^{+6}_{-6}	143^{+11}_{-12}	114^{+5}_{-5}	114^{+7}_{-8}
0.131	56^{+6}_{-6}	56^{+7}_{-7}	59^{+30}_{-31}	59^{+30}_{-31}

Note. These estimates of intrinsic FWHM correspond to directions along the major and minor axes of the scattering kernel. We give uncertainties for both the assumed characteristic scattering parameters (which only account for $\pm 1\sigma$ measurement uncertainties) and for the full range of plausible scattering parameters (which account for remaining uncertainties in the scattering kernel). We omit the estimated intrinsic minor axis at 3.6 cm because the minor axis scattering was estimated from this measurement (see Section 5.1).

requires density fluctuations of order unity. Suppose that the scattering material is statistically homogeneous over a region of length z along the line of sight. Electron density fluctuations $\delta n_{\mathrm{e}}(\ell)$ on a scale ℓ then introduce corresponding screen phase fluctuations of $\delta \phi(\ell) \sim r_{\mathrm{e}} \lambda \sqrt{\ell z} \, \delta n_{\mathrm{e}}(\ell)$ (because of the random walk through z/ℓ regions; see Section 2.1). Taking $\delta n_{\mathrm{e}}(\ell)/n_{\mathrm{e}} \sim (\ell/r_{\mathrm{out}})^{(\alpha-1)/2}$, we obtain,

$$\delta\phi(\ell) \sim n_{\mathrm{e}} \lambda r_{\mathrm{e}} \sqrt{z\ell} \left(\frac{\ell}{r_{\mathrm{out}}}\right)^{(\alpha-1)/2},$$

$$\Rightarrow r_{\mathrm{out}} \lesssim (n_{\mathrm{e}} \lambda r_{\mathrm{e}} \sqrt{z r_{\mathrm{diff}}})^{2/(\alpha-1)} r_{\mathrm{diff}}, \qquad (7)$$

where $r_{\mathrm{diff}} \approx \lambda/((1+M)\theta_{\mathrm{scatt}})$ is the diffractive scale (i.e., $\delta\phi(r_{\mathrm{diff}}) \sim 1$). For Sgr A*, $r_{\mathrm{diff}} \approx 10^{8}$ cm at $\lambda = 1$ cm. With
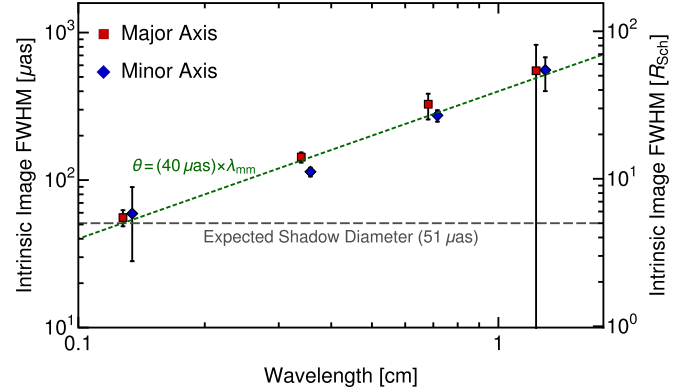

Figure 13. Estimated intrinsic size of Sgr A* along the directions of the major and minor axes of the scattering kernel. The error bars denote the range of values accounting for uncertainties in the full scattering model and for $\pm 1\sigma$ measurement uncertainty (see Table 1). Diamonds show central values for measured parameters and they use our recommended characteristic values for α and r_{in}. The major/minor axis markers are offset slightly in wavelength, for visual clarity. We also show the expected diameter of the black hole "shadow" and plot a simple isotropic source model with size directly proportional to wavelength. We do not find evidence for significant intrinsic anisotropy at any wavelength or for a steep scaling of intrinsic size with wavelength.

our characteristic value $\alpha = 1.38$, we then find

$$r_{\mathrm{out}} \lesssim (10 \text{ pc}) \times \left(\frac{n_{\mathrm{e}}}{10 \text{ cm}^{-3}}\right)^{5.26} \left(\frac{z}{10 \text{ pc}}\right)^{2.63}. \qquad (8)$$

For comparison, Armstrong et al. (1995) estimate $r_{\mathrm{out}} \gtrsim 30$ pc for the scattering material within 1 kpc. For Equation (8) to violate our measured lower limit for the 3.6 cm refractive noise would require much lower electron densities $n_{\mathrm{e}} \lesssim 0.1$ or larger values of α (approximately $\alpha \gtrsim 5/3$, for the characteristic

17

values of z and n_e given in Equation (8)), although these results are highly sensitive to the screen thickness, z. From the dispersion measure of the Galactic Center magnetar (e.g., Eatough et al. 2013; Kravchenko et al. 2016), we can only estimate an upper bound on the plasma density, $n_e < (180\ \mathrm{cm}^{-3})/(z/10\ \mathrm{pc})$. Regardless, the outer scale required by our scattering model is not implausible.

Goldreich & Sridhar (2006) have also provided an alternative model for interstellar scattering from folded magnetic field structures. Their proposed model reproduces the λ^2 scaling and Gaussian scatter-broadening for Sgr A*, but it also predicts significantly suppressed refractive scintillation. Furthermore, intrinsic structure would be blurred out on small angular scales from the scattering in this model. Thus, our measurements of image substructure at 1.3 cm conclusively reject the folded field model for the scattering of Sgr A* in its simplest form. However, we will demonstrate later that this model is compatible with our measurements if the inner scale (corresponding to the thickness of current sheets in this model) is significantly larger than expected: $r_{in} \sim 2 \times 10^6$ km. In this case, the Goldreich & Sridhar (2006) spectrum would instead produce significantly *enhanced* refractive effects at millimeter wavelengths.

6.2.2. The Inner Scale of Turbulence

Our measurements constrain the inner scale of turbulence, both through plausibility arguments related to the λ^2 dependence of the angular broadening and image Gaussianity and by relating the scattering power on large scales (refractive noise) to that on small scales (the diffractive blurring). Ultimately, our most stringent lower limit on the inner scale comes from the image Gaussianity at 1.3 cm, giving $r_{in} \gtrsim 600$ km. Likewise, the 7 mm data show a statistically significant departure from a Gaussian image, with a preference for $r_{in} \lesssim 1000$ km, although we regard this upper limit as tentative (see Section 5.2.4). Thus, we have adopted a recommended characteristic value of $r_{in} = 800$ km. While the scattering of Sgr A* is anomalously strong, the dissipation mechanism for turbulence in the ISM may be universal. Thus, we now compare our estimate for r_{in} with previous theoretical and observational estimates.

Using VLBI measurements of the angular broadening for several heavily scattered objects, Spangler & Gwinn (1990) estimated an inner scale of 50–200 km. Based on weak scintillation measurements at centimeter wavelengths, Armstrong et al. (1995) constrained the inner scale for the nearby ISM (within 1 kpc) to be less than $\sim 5 \times 10^4$ km. Rickett et al. (2009) estimated $r_{in} = 70$–100 km from the pulse-broadening of PSR J1644-4559. Smirnova & Shishov (2010) estimated $r_{in} = 350 \pm 150$ km from the pulse-broadening of PSR B2111+46. Each of these studies has its own limitations. For instance, the pulsar analyses assumed isotropic scattering, and Rickett et al. (2009) noted that a (finely tuned) anisotropy would allow an arbitrarily large inner scale. Perhaps the most significant difficulty in our study of Sgr A* is that intrinsic source structure becomes significant for the baselines and wavelengths that are sensitive to a direct estimate of the inner scale for Sgr A*. Nevertheless, our lower limit on the inner scale is quite robust.

Goldreich & Sridhar (1995) suggest that the inner scale in the ISM may approach the ion Larmor radius, and Spangler & Gwinn (1990) propose that the inner scale corresponds to the

larger of the ion inertial length and the ion Larmor radius in the scattering medium. The ion inertial length is $\ell_i = V_A/\Omega_i \approx 230/\sqrt{n_e/\mathrm{cm}^{-3}}$ km, where $V_A = B/\sqrt{4\pi n_e m_i}$ is the Alfvén speed and $\Omega_i = eB/(m_i c)$ is the ion cyclotron frequency. The ion Larmor radius is $r_i = v_{th}/\Omega_i \approx 930$ km $\times \left(\frac{B}{1\ \mu G}\right)^{-1}\left(\frac{T}{10^4\ \mathrm{K}}\right)^{1/2}$, where $v_{th} = \sqrt{kT/m_i}$ is the ion thermal speed. Given the strong scattering of Sgr A*, it is likely that the ion Larmor radius will then determine the inner scale in this model. The required $B \sim 1\ \mu G$ is somewhat lower than expected for magnetic fields in the ISM at the Galactocentric distance $R \sim 5.5$ kpc (e.g., Han et al. 2006), and it may suggest that the inner scale is a few times larger than r_i.

In terms of a specific model for the scattering of Sgr A*, Sicheneder & Dexter (2017) have proposed that the scattering may arise in a single H II region along the line of sight, with density $n_e \sim 200\ \mathrm{cm}^{-3}$ and radius ~ 3 pc. They note that this region can also produce the observed rotation measure of the Galactic Center magnetar SGR J1745-2900, if the field strengths in the scattering material are 15–70 μG. In this model, the ion inertial length is only $\ell_i \sim 10$–20 km and the ion Larmor radius is $r_i \lesssim 60$ km. Thus, our estimates of an inner scale that is significantly higher than either of these values support the scenario in which the large rotation measure (RM) of the magnetar arises from a local contribution near the Galactic Center (Eatough et al. 2013; Desvignes et al. 2018). For smaller magnetic fields, $B \sim 1\ \mu G$, the parameters identified by Sicheneder & Dexter (2017) remain plausible for the scattering.

6.2.3. The Power-law Index of Turbulence

Figure 14 shows our constraints on the power spectrum of phase fluctuations, $Q(\mathbf{q})$, along the direction of the scattering major axis. Refractive noise on a long baseline $\mathbf{u}$ is dominated by refractive modes with $\mathbf{q} \sim 2\pi\mathbf{u}/D$. Thus, our measurements of refractive noise at 3.6 and 1.3 cm constrain the power in wavenumbers $q^{-1} \sim 10^{13}$–10^{14} cm. In addition, our measurements of the asymptotic Gaussian angular broadening constrain the power in wavenumbers $q^{-1} \sim r_{in}$, with the exact constraint also weakly dependent on α: $Q(r_{in}^{-1}) \propto r_{in}^4/\Gamma(1 - \alpha/2)$.

As is evident from Figure 14, larger values of the inner scale require a flatter power spectrum for the measured refractive noise to be compatible with the measured angular broadening (see also Figure 9). Allowing arbitrarily small inner scales, we find $\alpha \lesssim 1.6$, while including our derived constraints on the inner scale, we obtain $\alpha < 1.47$. Thus, a Kolmogorov spectrum ($\alpha = 5/3$) is incompatible with our measurements, as is an $\alpha = 3/2$ spectrum (see, e.g., Iroshnikov 1964; Kraichnan 1965; Sridhar & Goldreich 1994; Goldreich & Sridhar 1995). Our results are at odds with measurements for the local ISM (e.g., Armstrong et al. 1995), the wavelength dependence of pulsar temporal broadening (e.g., Löhmer et al. 2001; Bhat et al. 2004; Lewandowski et al. 2013), and VLBI of heavily scattered sources (Spangler & Gwinn 1990), all of which tend to infer somewhat larger values of α. We now outline possible generalizations to our scattering model that might render higher values of α, including a Kolmogorov spectrum, feasible.

The first possibility is an outer scale of turbulence that is similar to the scales probed at 3.6 cm, thereby reducing the 3.6 cm refractive noise but perhaps not the 1.3 cm refractive noise (which probes smaller scales). The 3.6 cm refractive
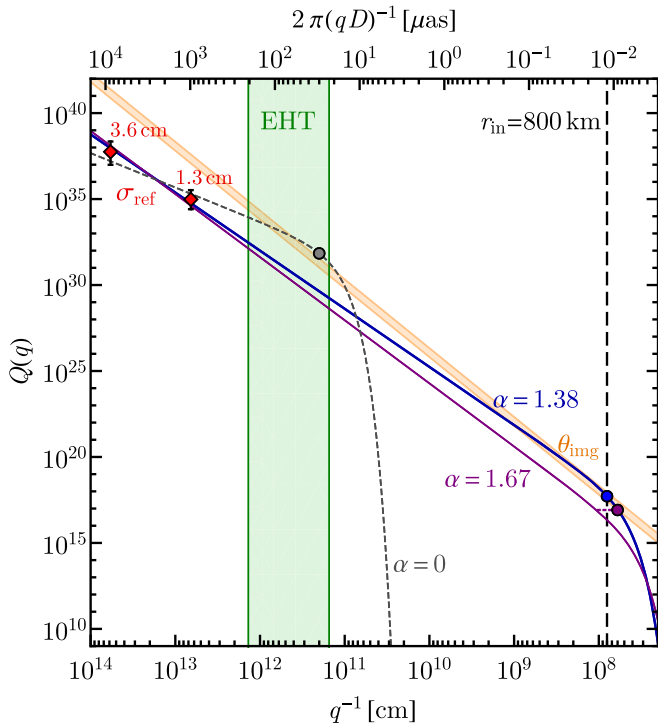
Figure 14. Summary of constraints on the power spectrum of phase fluctuations, $Q(\boldsymbol{q})$. Refractive noise on long baselines at 3.6 and 1.3 cm constrains the power in wavenumbers $q^{-1} \sim 10^{13}$–10^{14} cm (red diamonds). Asymptotic Gaussian angular broadening constrains the power in wavenumbers $q \sim r_{in}^{-1}$; the corresponding constraint on Q depends strongly on r_{in} and weakly on α. The orange band shows the angular broadening constraint as a function of $q = r_{in}^{-1}$ over the range $1 < \alpha < 5/3$. Three models are plotted: a Kolmogorov spectrum with our minimum allowed inner scale (purple; $\alpha = 5/3$, $r_{in} = 600$ km), our recommended characteristic model (blue; $\alpha = 1.38$, $r_{in} = 800$ km), and a Goldreich & Sridhar (2006) spectrum (dashed gray; $\alpha = 0$, $r_{in} = 2 \times 10^6$ km). Corresponding colored circles show the constraint on Q from angular broadening for each model. While a Kolmogorov spectrum is compatible with the refractive noise measurements taken alone, it would require spectral flattening or additional power near the inner scale to be compatible with the measured angular broadening, as shown by the horizontal purple dashed line. The green shaded region shows the range of modes that contribute refractive noise to EHT images of Sgr A* ($\sigma_{ref} \propto \sqrt{Q}$). Note that refractive noise predictions from our model for the EHT are rather insensitive to possible generalizations that would allow $\alpha = 5/3$. However, the Goldreich & Sridhar (2006) spectrum would increase refractive noise by a factor of ≈ 10 relative to our characteristic model.

noise corresponds to scattering modes with a transverse scale of ~ 4 au on the scattering screen, so the required outer scale is $r_{out} \sim 1$ au. This value is somewhat smaller than the lower limit estimated by Armstrong et al. (1995). Moreover, this is a finely tuned constraint, requiring the outer scale to be precisely matched to our observing parameters—a smaller outer scale would be inconsistent with the observed 1.3 cm refractive noise, and a larger outer scale would not affect the 3.6 cm noise.

A second possibility is that there is extra power located near the dissipation scale. Spectral flattening near the inner scale has been seen in the solar wind (e.g., Neugebauer 1975; Celnikier et al. 1983; Coles et al. 1991) and possibly also in the ISM (Smirnova & Shishov 2010). A pile-up in power by a factor of ~ 15 would reconcile our measurements with a Kolmogorov spectrum (see Figure 14); a factor of ≈ 2 would be needed for an $\alpha = 3/2$ spectrum.

A more radical possibility, which is not excluded by our data, is that the spectrum is extremely shallow and the inner

scale is correspondingly large. In particular, the model of Goldreich & Sridhar (2006) produces a power spectrum with $\alpha = 0$, which would be consistent with all our measurements if $r_{in} \sim 2 \times 10^6$ km. This inner scale is a factor of 20 larger than the characteristic value used by Goldreich & Sridhar (2006) and requires an outer scale that is 400 times larger than expected, or a few kpc. Nevertheless, our measurements are insufficient to rule out this type of power spectrum, and it would produce refractive signatures for the EHT that are approximately 10 times stronger than those predicted by our recommended characteristic model. Thus, we expect continued studies at 1.3 mm (and possibly 3.5 mm) will be able to conclusively confirm or reject this scattering model for Sgr A*.

6.3. Sensitivity to the Assumed Scattering Model

We have analyzed all our data in the context of a single scattering model. The anisotropy in this model is determined by the magnetic field wander along the line of sight relative to its preferred orientation (which determines the minor axis of the scattering ellipse). Psaltis et al. (2018) give three representative models for the field wander: "von Mises," "Dipole," and "Boxcar." The von Mises model represents the angular field wander using a generalized Gaussian distribution for circular quantities, the Dipole model uses a change of variables to rescale the principal axes of the power spectrum, and the Boxcar model has a power spectrum that is isotropic across a restricted range of angles and is zero elsewhere. Because of the efficient computational tools developed in Appendix B, all of our results have used the Dipole model. We now evaluate how sensitive our conclusions are to this choice.

Psaltis et al. (2018) show that the shape of the scattering kernel is almost independent of the choice of scattering model. However, the refractive noise along the minor axis is sensitive to the scattering model. Because our measurements of refractive noise are predominantly along the major axis, our results are not strongly affected by the choice of scattering model.

For example, the mean refractive noise on our long baselines at 3.6 cm changes by less than $\pm 2\%$ among the three scattering models (well within our uncertainty from sampling only a few elements of the refractive noise). Likewise, the 95% confidence intervals are almost identical for the three models. For the average refractive noise on long baselines at 1.3 cm, the von Mises and Dipole models agree to within 1%, but the Boxcar model differs by 5%. Again, these differences are negligible within our error budget.

Thus, we conclude that our specific choice of scattering model is irrelevant for our results. Equivalently, our current measurements provide no firm guidance for discriminating among these models for the magnetic field wander. Future measurements of refractive noise on long baselines along the minor axis could immediately rule out the Boxcar model and would be sensitive to differences between the von Mises and Dipole models (see, e.g., Figures 9 and 13 in Psaltis et al. 2018).

6.4. Implications for Continued Studies of Sgr A*

For the scattering parameters that we have identified, a Gaussian scattering kernel is likely a good approximation for Sgr A* for centimeter wavelengths, although the full non-Gaussian kernel shape should be used for continued studies at
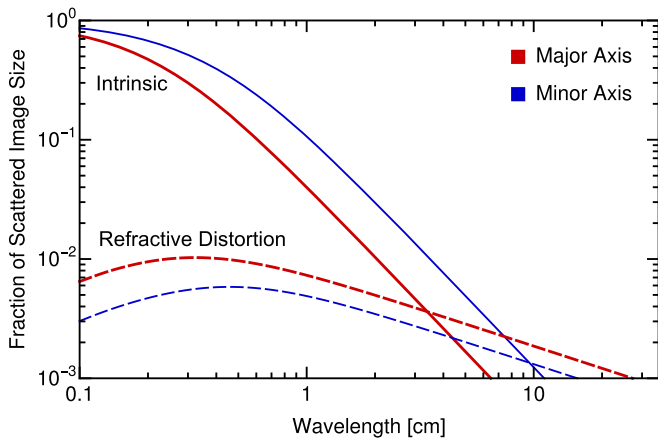
Figure 15. Comparison of the wavelength-dependent fractional effects from intrinsic image structure and from refractive image distortion. The intrinsic curves show the fractional increase in the scattered image size because of intrinsic structure: $1 - \theta_{\mathrm{scatt}}/\theta_{\mathrm{ea}}$, where θ_{scatt} is the size of a scattered point source and θ_{ea} is the angular size of an extended source using our estimated wavelength-dependent size of Sgr A*. The refractive distortion curves show the expected fractional fluctuations of image size among different observing epochs because of refractive scattering (see Section 5.2.2). Intrinsic structure can only be reliably estimated when refractive jitter is significantly smaller than the intrinsic contribution, irrespective of the observing sensitivity or baseline coverage. Requiring that the fractional increase from intrinsic size must be at least three times the rms distortion, we estimate that intrinsic properties for the major axis can only be reliably constrained for observations with $\lambda \lesssim 1.3$ cm, while intrinsic properties for the minor axis can only be constrained for observations with $\lambda \lesssim 3.6$ cm.

millimeter wavelengths. The full kernel shape is especially important for scattering mitigation in imaging with EHT data (Fish et al. 2014; Johnson 2016).

We have shown that refractive noise is a critical component of the error budget when model fitting to observations of Sgr A*. In addition, we caution that inferences of intrinsic size should account for refractive image distortion. At long wavelengths, stochastic changes from refractive distortion can exceed the contribution of intrinsic structure (see Figure 15). Our results suggest that intrinsic structure can only be securely decoupled from refractive distortion for $\lambda \lesssim 3.6$ cm (minor axis) or $\lambda \lesssim 1.3$ cm (major axis). Note that these are fundamental limitations; they would apply even if the sensitivity and baseline coverage of the observations were perfect.

Our work has two significant implications for imaging Sgr A* with the EHT. First, we have shown that the scattering kernel may be much smaller than has been estimated, so the blurring effects of scattering may be less severe than have been assumed (see Figure 12). Second, we find $\alpha \lesssim 1.47$, which produces significantly less refractive noise than the standard Kolmogorov picture; it predicts that the renormalized refractive noise is at most $\sim 1\%$ of the zero-baseline flux density (see Figure 16). This estimate reinforces the conclusions of Fish et al. (2016) and Lu et al. (2018) that refractive noise is unlikely to be a significant component of the error budget for past EHT observations. Both these implications improve the prospects for horizon-scale imaging at 1.3 mm. However, continued observations must also account for the possibility of strong refractive effects from shallow spectra, such as from the model with $\alpha = 0$ and $r_{\mathrm{in}} = 2 \times 10^6$ km. While this model remains speculative and lacks support from other lines of sight, it would produce striking differences from our characteristic model for EHT observations (an increase in refractive noise by
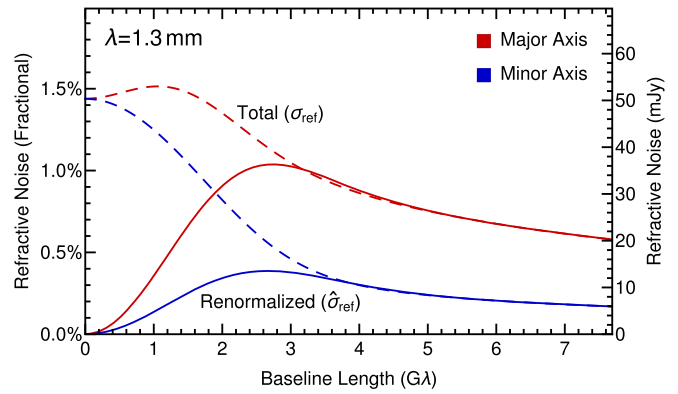

Figure 16. Expected rms of refractive noise (dashed) and renormalized refractive noise (solid) for Sgr A* at 1.3 mm (i.e., for EHT observations). The curves correspond to our recommended characteristic scattering model and an isotropic intrinsic Gaussian source with FWHM $\theta_{\mathrm{src}} = 52~\mu$as. To express the refractive noise in units of flux density, we assume a total flux density of 3.5 Jy for Sgr A*.

a factor of 10) and should be tested further with long-baseline measurements at 1.3 mm and 3.5 mm.

7. Summary

We have analyzed observations of Sgr A* at wavelengths from 1.3 mm to 30 cm using a physically motivated model for its scattering (developed in Psaltis et al. 2018). At long wavelengths, the angular broadening from scattering is an anisotropic Gaussian, and its size scales as $\theta_{\mathrm{scatt}} \propto \lambda^2$. At shorter wavelengths, the shape and wavelength dependence of the scattering depend on the inner scale of turbulence, r_{in}, and on the power-law index of the scattering, α. Using a new prescription to perform model fitting with refractive noise in the error budget, we are able to estimate the asymptotic Gaussian scattering parameters to excellent accuracy (see Table 2). In addition, we show that $\alpha \lesssim 1.47$ and $r_{\mathrm{in}} \gtrsim 600$ km (our recommended characteristic values for these parameters are $\alpha = 1.38$ and $r_{\mathrm{in}} = 800$ km). Our recommended scattering parameters are summarized in Table 3.

After deconvolving the effects of scattering from our estimated sizes of the scatter-broadened images, we find that the intrinsic image of Sgr A* is nearly isotropic, with FWHM $\theta_{\mathrm{src}} \sim (40~\mu$as$) \times \lambda_{\mathrm{mm}}$ from 1.3 mm to 1.3 cm. While this linear wavelength dependence for the emission size is natural for both disk- and jet-dominated models, the nearly isotropic image shape strongly favors disk models. At 1.3 mm, where the emission region is expected to be largely optically thin, our estimated image size is consistent with predictions from recent GRRMHD simulations (e.g., Chael et al. 2018).

For ISM scattering, our most surprising conclusion is that a Kolmogorov spectrum ($\alpha = 5/3$) in the inertial range is incompatible with our observations. However, our constraints on α are somewhat indirect, as they relate the refractive power in large scattering modes to the diffractive power from small scattering modes (see Figure 14). For a generalized scattering model, larger values of α are possible but would require continuous injection of energy on $\lesssim$au-scales, a pile-up of energy near the inner scale ($\sim 10^3$ km), or a small outer scale for the turbulence (~ 1 au).

We have also shown that the inner scale cannot be smaller than 600 km and is likely $r_{\mathrm{in}} \approx 800$ km. This scale is comparable to the ion Larmor radius for regions of the ISM

with weak magnetic fields $B \sim 1\,\mu G$, thereby supporting identification of the ion Larmor radius (or a few times this radius) with the dissipation scale of ISM turbulence. This estimate also suggests that the rotation measure associated with the scattering material is modest, and hence that the rotation measure of the Galactic Center magnetar is dominated by local contributions (Eatough et al. 2013) rather than from the scattering material (Sicheneder & Dexter 2017). Our estimated r_{in} is also comparable to the ion inertial length for $n_e \sim 0.1\,cm^{-3}$ and requires $n_e \gtrsim 0.1\,cm^{-3}$ if the inner scale is determined by the larger of these characteristic two plasma length scales (Spangler & Gwinn 1990). However, we cannot conclusively rule out much shallower spectra with correspondingly larger inner scales.

While our primary objective has been to constrain the parameters of our specific scattering model, our observations also constrain alternative theories for the scattering of Sgr A*. For example, Goldreich & Sridhar (2006) have proposed a model in which the scattering is caused by an ensemble of folded current sheets in the ISM. While this model naturally reproduces the λ^2 scaling of angular broadening and the Gaussian image at long radio wavelengths, it predicts an absence of refractive scattering effects. This model would not produce scattering substructure in images, and any intrinsic substructure would be blurred out by small-scale scattering modes. Hence, the pronounced long-baseline refractive noise at 1.3 cm enables us to firmly reject this alternative scattering model for Sgr A* in its simplest form (see also Gwinn et al. 2014). However, the model is compatible with our measurements if the thickness of the current sheets is significantly larger than expected, corresponding to $r_{in} \sim 2 \times 10^6\,km$, in which case it would instead produce strongly *enhanced* refractive effects at millimeter wavelengths. Thus, we expect that continued observations with the Global 3 mm VLBI Array (GMVA) and EHT will be sufficient to firmly support or reject this model.

Our results highlight the importance of including refractive noise when fitting models to radio observations of Sgr A*. Refractive uncertainties can plausibly explain many of the discrepancies in past measurements of the size of Sgr A*, such as those identified by Psaltis et al. (2015b). In addition, we have shown that refractive effects likely prohibit a meaningful study of intrinsic structure at wavelengths longer than 1.3 cm (or 3.6 cm for the minor axis; see Figure 15). Nevertheless, our results also show that both the blurring and substructure from scattering may be significantly smaller at 1.3 mm than expected. Thus, the prospects for deeper study of Sgr A* at millimeter wavelengths, including imaging with the EHT, are excellent.

Appendix A
Calculating Renormalized Refractive Noise

As described in Section 2.2, refractive noise includes contributions that may not be appropriate for the relevant error budget. For instance, the refractive noise on a zero-baseline corresponds to refractive modulation of the total flux density, which may be absorbed into model parameters. Likewise, the variance in the imaginary part of visibilities on short baselines is produced by image wander, which is only relevant for observations with absolute phase referencing. We now derive "renormalized" refractive noise expressions, which remove the contributions of flux density modulation and/or image wander. We derive expressions to efficiently compute properties of renormalized refractive noise semi-analytically, following the methodology and notation of Johnson & Narayan (2016) (see also Blandford & Narayan 1985).

To proceed, we will first define the renormalized average visibility $\hat{V}_a(\boldsymbol{b})$ as the visibility corresponding to a scattered image that has been normalized to have unit total flux density (e.g., $\hat{V}_a(0) = 1$) and that has been shifted such that its brightness distribution is centered on the origin:

$$
\begin{aligned}
\hat{V}_a(\boldsymbol{b}) &\equiv \frac{V_a(\boldsymbol{b})}{V_a(0)} e^{2\pi i \boldsymbol{b}\cdot\boldsymbol{x}_{0,a}/(\lambda D)} \\
&= \frac{V_{ea}(\boldsymbol{b}) + \Delta V_a(\boldsymbol{b})}{V_{ea}(0) + \Delta V_a(0)} e^{2\pi i \boldsymbol{b}\cdot\Delta\boldsymbol{x}_{0,a}/(\lambda D)} e^{2\pi i \boldsymbol{b}\cdot\boldsymbol{x}_{0,ea}/(\lambda D)} \\
&\approx \frac{e^{2\pi i \boldsymbol{b}\cdot\boldsymbol{x}_{0,ea}/(\lambda D)}}{V_{ea}(0)} \Big[V_{ea}(\boldsymbol{b}) + \Delta V_a(\boldsymbol{b}) \\
&\quad - \frac{V_{ea}(\boldsymbol{b})}{V_{ea}(0)} \Delta V_a(0) + 2\pi i V_{ea}(\boldsymbol{b})\boldsymbol{b}\cdot\Delta\boldsymbol{x}_{0,a}/(\lambda D) \Big]. \quad (9)
\end{aligned}
$$

In these expressions and throughout the remainder of this paper, a subscript "a" denotes a quantity in the average image regime, while "ea" denotes a quantity in the ensemble-average image regime (Goodman & Narayan 1989; Narayan & Goodman 1989). The original image centroid, $\boldsymbol{x}_{0,a}$, is given as a transverse displacement on the scattering screen. Thus, in angular units, the centroid is at $\boldsymbol{\eta}_{0,a} \equiv \boldsymbol{x}_{0,a}/D$. We assume that the refractive effects are only a small perturbation of the ensemble-average image, so the final expression only includes refractive terms to linear order.

The renormalized refractive noise can then be written

$$
\begin{aligned}
\Delta\hat{V}_a(\boldsymbol{b}) &\approx \frac{e^{2\pi i \boldsymbol{b}\cdot\boldsymbol{x}_{0,ea}/(\lambda D)}}{V_{ea}(0)} \Big[\Delta V_a(\boldsymbol{b}) - \frac{V_{ea}(\boldsymbol{b})}{V_{ea}(0)} \Delta V_a(0) \\
&\quad + 2\pi i V_{ea}(\boldsymbol{b})\boldsymbol{b}\cdot\Delta\boldsymbol{x}_{0,a}/(\lambda D) \Big].
\end{aligned} \quad (10)
$$

The prefactor in this expression only depends on the ensemble-average visibility. It normalizes the ensemble-average image to

have unit flux density and to be centered on the origin. The first term inside the square brackets is the full refractive noise of the average image. The remaining two terms remove the contributions from flux modulation and from image wander, respectively. To simplify the remainder of our discussion, we will assume that the ensemble-average image is centered on the origin: $x_{0,\text{ea}} = 0$ and $\Delta x_{0,\text{a}} = x_{0,\text{a}}$.

To estimate properties of the refractive noise, we must determine the function $f_{\hat{V}}(r; b, \lambda)$ defined by $\Delta \hat{V}_a(b) \equiv \int d^2 r \, f_{\hat{V}}(r; b, \lambda)\phi(r)$, where $\phi(r)$ is the refractive component of the scattering screen phase (i.e., consisting only of modes with wavelengths longer than the Fresnel scale). For example, the average visibility is approximated as (see Johnson & Narayan 2016, Equations (11) and (12))

$$V_a(b) \approx V_{\text{ea}}(b) + \int d^2 r \, f_V(r; b, \lambda)\phi(r) \equiv V_{\text{ea}}(b) + \Delta V_a(b),$$

$$f_V(r; b, \lambda) \equiv r_F^2 e^{-ir \cdot b/(D\lambda)} \left[\frac{i}{D\lambda} b \cdot \nabla I_{\text{ea}}(r) - \nabla^2 I_{\text{ea}}(r) \right]. \tag{11}$$

These equations arise from the approximate representation of scattering in the geometric optics regime, which gives the scattered image $I_a(r)$ in terms of the ensemble-average image $I_{\text{ea}}(r)$ and the refractive scattering screen phase gradients:

$$I_a(r) \approx I_{\text{ea}}(r + r_F^2 \nabla \phi_r(r))$$
$$\approx I_{\text{ea}}(r) + r_F^2 [\nabla \phi_r(r)] \cdot [\nabla I_{\text{ea}}(r)]. \tag{12}$$

To denote the integral correspondence in Equation (11), we will introduce the shorthand $\Delta V_a(b) \leftrightarrow f_V(r; b, \lambda)$. Obviously, we then have $\Delta V_a(0) \leftrightarrow f_V(r; 0, \lambda)$. Finally, note that

$$\nabla_b V_a(b)|_{b=0} = -2\pi i V_a(0) x_{0,\text{a}}/(\lambda D)$$
$$= -2\pi i V_a(0) \Delta x_{0,\text{a}}/(\lambda D), \tag{13}$$

where ∇_b denotes a gradient with respect to the baseline (not the directional derivative $b \cdot \nabla$). This general identity relates an image centroid to the corresponding visibility gradient at zero baseline. We will use the notation that $\nabla_b V_a(b)|_{b=0} \equiv \nabla_{b=0} V_a(b)$. Thus, $\Delta x_{0,\text{a}} = i \frac{\lambda D}{2\pi} \frac{1}{V_a(0)} \nabla_{b=0} V_a(b) \approx i \frac{\lambda D}{2\pi} \frac{1}{V_{\text{ea}}(0)} \nabla_{b=0} V_a(b)$. Consequently,

$$\Delta x_{0,\text{a}} \leftrightarrow i \frac{\lambda D}{2\pi} \frac{1}{V_{\text{ea}}(0)} \nabla_{b=0} f_V(r; b, \lambda). \tag{14}$$

Putting everything together, we obtain

$$\Delta \hat{V}_a(b) \leftrightarrow f_{\hat{V}}(r; b, \lambda) \equiv \frac{1}{V_{\text{ea}}(0)}$$
$$\times \left[f_V(r; b, \lambda) - \frac{V_{\text{ea}}(b)}{V_{\text{ea}}(0)} f_V(r; 0, \lambda) \right.$$
$$\left. - \frac{V_{\text{ea}}(b)}{V_{\text{ea}}(0)} b \cdot \nabla_{b=0} f_V(r; b, \lambda) \right]. \tag{15}$$

For computational purposes, we require the Fourier-conjugate quantity, $\tilde{f}_{\hat{V}}(q; b, \lambda) \equiv \int d^2 r \, f_{\hat{V}}(r; b, \lambda) e^{-iq \cdot r}$, which follows

trivially from Equation (15):

$$\tilde{f}_{\hat{V}}(q; b, \lambda) = \frac{1}{V_{\text{ea}}(0)}$$
$$\times \left[\tilde{f}_V(q; b, \lambda) - \frac{V_{\text{ea}}(b)}{V_{\text{ea}}(0)} \tilde{f}_V(q; 0, \lambda) \right.$$
$$\left. - \frac{V_{\text{ea}}(b)}{V_{\text{ea}}(0)} b \cdot \nabla_{b=0} \tilde{f}_V(q; b, \lambda) \right], \tag{16}$$

where $\tilde{f}_V(q; b, \lambda)$ is (Johnson & Narayan 2016, Equation (15))

$$\tilde{f}_V(q; b, \lambda) = r_F^2 q \cdot [q + (1 + M)^{-1} r_F^{-2} b]$$
$$\times V_{\text{ea}}((1 + M) r_F^2 q + b). \tag{17}$$

As in Equation (10), the prefactor in Equation (16) normalizes the ensemble-average image to have unit total flux density. The first term in the brackets gives the usual contribution of refractive noise, the second term eliminates noise from refractive flux modulation, and the third term eliminates noise from refractive position wander.

We can also express Equation (16) explicitly in terms of the ensemble-average visibility and its gradient:

$$b \cdot \nabla_{b=0} \tilde{f}_V(q; b, \lambda) = \frac{q \cdot b}{1 + M} V_{\text{ea}}((1 + M) r_F^2 q)$$
$$+ r_F^2 |q|^2 b \cdot \nabla V_{\text{ea}}((1 + M) r_F^2 q)$$
$$\Rightarrow \tilde{f}_{\hat{V}}(q; b, \lambda) = \frac{r_F^2}{V_{\text{ea}}(0)} \{ q \cdot [q + (1 + M)^{-1} r_F^{-2} b]$$
$$\times \left[V_{\text{ea}}((1 + M) r_F^2 q + b) - \frac{V_{\text{ea}}(b)}{V_{\text{ea}}(0)} V_{\text{ea}}((1 + M) r_F^2 q) \right]$$
$$- |q|^2 \frac{V_{\text{ea}}(b)}{V_{\text{ea}}(0)} b \cdot \nabla V_{\text{ea}}((1 + M) r_F^2 q) \}. \tag{18}$$

In this expression, the terms that eliminate flux modulation and image wander are mixed.

A benefit of these representations is that we can easily calculate the corresponding functions for the real or imaginary components of the normalized refractive noise; e.g., $\text{Re}[\Delta \hat{V}_a(b)] \leftrightarrow f_{\hat{V},\text{re}}(r; b, \lambda)$. These functions are necessary to estimate the full covariance matrix of the complex refractive noise among different interferometric baselines. Specifically, because $f_{\hat{V}}(r; -b, \lambda) = f_{\hat{V}}^*(r; b, \lambda)$ and the Fourier transform is linear, we obtain

$$\tilde{f}_{\hat{V},\text{re}}(q; b, \lambda) = \frac{1}{2} [\tilde{f}_{\hat{V}}(q; b, \lambda) + \tilde{f}_{\hat{V}}(q; -b, \lambda)],$$
$$\tilde{f}_{\hat{V},\text{im}}(q; b, \lambda) = \frac{1}{2i} [\tilde{f}_{\hat{V}}(q; b, \lambda) - \tilde{f}_{\hat{V}}(q; -b, \lambda)]. \tag{19}$$

Using these functions, we can compute statistical properties of the renormalized refractive noise using the expressions given in Johnson & Narayan (2016), with $\tilde{f}_V$ replaced by $\tilde{f}_{\hat{V}}$. For example, the variance of the renormalized refractive noise on a baseline b is

$$\langle |\Delta \hat{V}_a(b)|^2 \rangle = \frac{\lambda^2}{(2\pi)^4} \int d^2 q \, |\tilde{f}_{\hat{V}}(q; b, \lambda)|^2 Q(q). \tag{20}$$
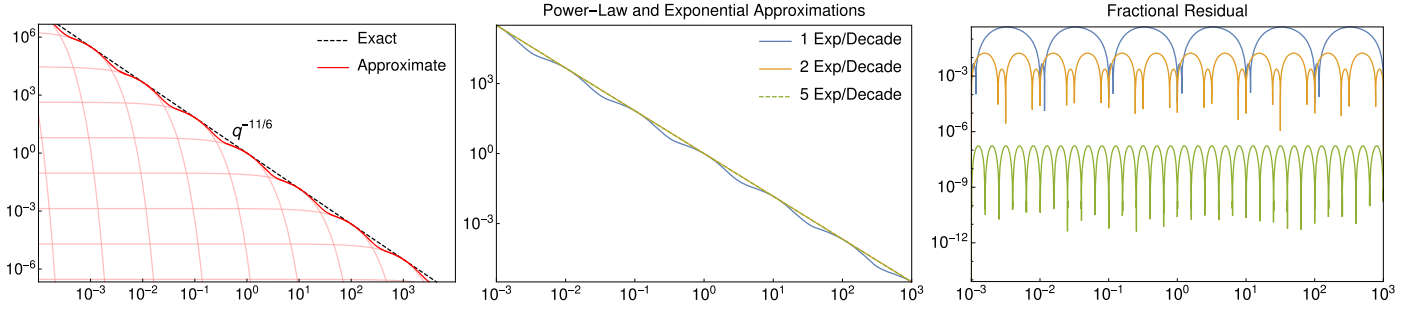
Figure 17. Approximating a power law using a sum of exponentials. In all panels, the exact power law is $q^{-11/6}$. The left panel shows how our exponential approximation is constructed; in this example, one exponential per decade is summed. Each of these components matches the power law and its derivative at the reference point, q_i, and (in log–log space) each has the form of a soft step function. The exponentials are then summed and normalized at the chosen global reference point (here, at $q = 1$). The center panel compares the approximations with one, two, and five exponentials per decade, and the right panel shows the fractional residual in each case.

Appendix B
Efficient Computation of Refractive Noise

Even the simplified expressions for refractive noise (e.g., Equation (20)) remain numerically expensive, and an efficient approximation is necessary for our fitting framework. We now derive a suitable approximation by making two key simplifications: we approximate the ensemble-average visibility as an elliptical Gaussian, and we approximate the power spectrum $Q(q) \propto q^{-(\alpha+2)}$ as a sum of exponentials. With these approximations, the (renormalized) refractive noise integrals (e.g., Equation (20)) become Gaussian integrals and can be computed analytically. The first of these approximations is likely excellent for Sgr A*; the second can achieve any desired accuracy based on a simple prescription that we now develop.

Specifically, we use the framework of Psaltis et al. (2018) to define the power spectrum of phase fluctuations in the scattering screen. In this framework, the power spectrum arises from a wandering magnetic field direction throughout the scattering medium; anisotropic scattering arises if the field has a preferred direction, with the major axis of the scattering orthogonal to the preferred field direction. In this framework, the power spectrum takes the form,

$$Q(\boldsymbol{q}) = \bar{Q} \, (q r_{\mathrm{in}})^{-(\alpha+2)} \exp(-q^2 r_{\mathrm{in}}^2) P(\phi_q - \phi_0), \quad (21)$$

where $P(\phi_q - \phi_0)$ describes the (normalized) angular distribution of scattering power, and the overall normalization $\bar{Q}$ is given by

$$\bar{Q} = \frac{2}{\Gamma\left(1 - \frac{\alpha}{2}\right)} \left[\frac{r_{\mathrm{in}}^2 (D + R)}{\frac{\sqrt{2 \ln 2}}{\pi} \lambda_0^2 R} \right]^2 (\theta_{\mathrm{maj},0}^2 + \theta_{\mathrm{min},0}^2). \quad (22)$$

We will use the "dipole" model of Psaltis et al. (2018):

$$P(\phi_q - \phi_{0,\mathrm{PA}}; k_\zeta) = \frac{[1 + k_\zeta \sin^2(\phi_q - \phi_{0,\mathrm{PA}})]^{-(\alpha+2)/2}}{2\pi \, {}_2F_1(1/2, 1 + \alpha/2; 1; -k_\zeta)}, \quad (23)$$

where k_ζ is determined by the asymptotic ($\lambda \to \infty$) asymmetry of the scatter-broadening:

$$\left(\frac{\theta_{\mathrm{maj},0}}{\theta_{\mathrm{min},0}} \right)^2 = \frac{{}_2F_1\left(\frac{\alpha+2}{2}, \frac{1}{2}; 2; -k_\zeta\right)}{{}_2F_1\left(\frac{\alpha+2}{2}, \frac{3}{2}; 2; -k_\zeta\right)}. \quad (24)$$

With this model, the power spectrum can be written

$$Q(\boldsymbol{q}) = \frac{\bar{Q} r_{\mathrm{in}}^{-(\alpha+2)}}{2\pi \, {}_2F_1(1/2, 1 + \alpha/2; 1; -k_\zeta)}$$
$$\times (q^2 [1 + k_\zeta \sin^2(\phi_q - \phi_{0,\mathrm{PA}})])^{-(\alpha+2)/2} \exp(-q^2 r_{\mathrm{in}}^2). \quad (25)$$

We can now derive an approximation of $Q(\boldsymbol{q})$ about some point $\boldsymbol{q}_0$. For this, we approximate a power law using a sum of exponentials (see also, e.g., Bochud & Challet 2007). Consider the function $f_{\mathrm{pl}}(q; z) = q^{-z}$. We will define an exponential basis function at a location q_i as

$$f_{\mathrm{exp}}(q; z, q_i) \equiv q_i^{-z} e^{-z\left(\frac{q}{q_i} - 1\right)}. \quad (26)$$

Note that the basis function and its first derivative match the power law at $q = q_i$: $f_{\mathrm{exp}}(q_i; z, q_i) = f_{\mathrm{pl}}(q_i; z)$ and $f_{\mathrm{exp}}'(q_i; z, q_i) = f_{\mathrm{pl}}'(q_i; z)$. To approximate $f_{\mathrm{pl}}(q; z)$, we sum exponential basis functions that are evenly spaced logarithmically over a desired range $\{q_{\mathrm{min}}, q_{\mathrm{max}}\}$; we then normalize the result so that the approximate and exact forms match at some reference coordinate q_{ref}. For instance, taking $q_{\mathrm{ref}} = 1$, we obtain

$$f_{\mathrm{pl}}(q; z) \approx f_{\mathrm{exp}}(q; z, \{q_i\}) \equiv \frac{\sum_{q_i} f_{\mathrm{exp}}(q; z, q_i)}{\sum_{q_i} f_{\mathrm{exp}}(1; z, q_i)}. \quad (27)$$

Figure 17 illustrates why this approximation is effective and shows the errors when one, two, and five exponentials are placed per decade in the range of interest. In essence, the exponential basis functions act as approximate step functions in log–log space; they are flat at values smaller than q_i and quickly approach zero at larger values.

We can thus approximate the power spectrum near a point $\boldsymbol{q}_0$ as

$$Q_{\mathrm{approx}}(\boldsymbol{q}; \boldsymbol{q}_0) \equiv \frac{\bar{Q}(q_0^2 r_{\mathrm{in}}^2 [1 + k_\zeta \sin^2(\phi_{q_0} - \phi_{0,\mathrm{PA}})])^{-(\alpha+2)/2}}{2\pi \, {}_2F_1(1/2, 1 + \alpha/2; 1; -k_\zeta)}$$
$$\times e^{-q^2 r_{\mathrm{in}}^2} f_{\mathrm{exp}}\left(\frac{q^2 [1 + k_\zeta \sin^2(\phi_q - \phi_{0,\mathrm{PA}})]}{q_0^2 [1 + k_\zeta \sin^2(\phi_{q_0} - \phi_{0,\mathrm{PA}})]}, -\frac{\alpha+2}{2} \right). \quad (28)$$
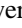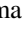
By normalizing the power law in this way, the function f_{exp} can be referenced to a value $q_{\mathrm{ref}} = 1$, with basis functions that

are independent of q. Note that the argument of $f_{\exp}$ is quadratic in q, and

$$
\begin{aligned}
q^2[1 + k_\zeta \sin^2(\phi_q - \phi_{0,\mathrm{PA}})] &= \left(1 + \frac{k_\zeta}{2}[1 - \cos(2\phi_{0,\mathrm{PA}})]\right) \\
&\times (q_x^2 + q_y^2) - k_\zeta q_x q_y \sin(2\phi_{0,\mathrm{PA}}).
\end{aligned}
\tag{29}
$$

Thus, the exponential approximation for $Q(q)$ (Equation (28)) yields a sum of Gaussian functions in q.

ORCID iDs

Michael D. Johnson ⓘ https://orcid.org/0000-0002-4120-3029
Dimitrios Psaltis ⓘ https://orcid.org/0000-0003-4058-2837
Lindy Blackburn ⓘ https://orcid.org/0000-0002-9030-642X
Yuri Y. Kovalev ⓘ https://orcid.org/0000-0001-9303-3263
Carl R. Gwinn ⓘ https://orcid.org/0000-0002-6936-4430
Guang-Yao Zhao ⓘ https://orcid.org/0000-0002-4417-1659
Geoffrey C. Bower ⓘ https://orcid.org/0000-0003-4056-9982
Motoki Kino ⓘ https://orcid.org/0000-0002-2709-7338
Michael Kramer ⓘ https://orcid.org/0000-0002-4175-2271
Kazunori Akiyama ⓘ https://orcid.org/0000-0002-9475-4254
Jason Dexter ⓘ https://orcid.org/0000-0003-3903-0373

References

Akiyama, K., Kino, M., Sohn, B., et al. 2014, in IAU Symp. 303, The Galactic Center: Feeding and Feedback in a Normal Galactic Nucleus, ed. L. O. Sjouwerman, C. C. Lang, & J. Ott (Cambridge: Cambridge Univ. Press), 288
Armstrong, J. W., Rickett, B. J., & Spangler, S. R. 1995, ApJ, 443, 209
Backer, D. C., Zensus, J. A., Kellermann, K. I., et al. 1993, Sci, 262, 1414
Balick, B., & Brown, R. L. 1974, ApJ, 194, 265
Bhat, N. D. R., Cordes, J. M., Camilo, F., Nice, D. J., & Lorimer, D. R. 2004, ApJ, 605, 759
Blandford, R., & Narayan, R. 1985, MNRAS, 213, 591
Blandford, R. D., & Königl, A. 1979, ApJ, 232, 34
Bochud, T., & Challet, D. 2007, QuFin, 7, 585
Bower, G. C., Deller, A., Demorest, P., et al. 2014a, ApJL, 780, L2
Bower, G. C., Deller, A., Demorest, P., et al. 2015a, ApJ, 798, 120
Bower, G. C., Falcke, H., Herrnstein, R. M., et al. 2004, Sci, 304, 704
Bower, G. C., Goss, W. M., Falcke, H., Backer, D. C., & Lithwick, Y. 2006, ApJL, 648, L127
Bower, G. C., Markoff, S., Brunthaler, A., et al. 2014b, ApJ, 790, 1
Bower, G. C., Markoff, S., Dexter, J., et al. 2015b, ApJ, 802, 69
Bower, G. C., Roberts, D. A., Yusef-Zadeh, F., et al. 2005, ApJ, 633, 218
Brinkerink, C. D., Müller, C., Falcke, H., et al. 2016, MNRAS, 462, 1382
Broderick, A. E., Fish, V. L., Doeleman, S. S., & Loeb, A. 2009, ApJ, 697, 45
Broderick, A. E., Fish, V. L., Johnson, M. D., et al. 2016, ApJ, 820, 137
Celnikier, L. M., Harvey, C. C., Jegou, R., Moricet, P., & Kemp, M. 1983, A&A, 126, 293
Chael, A., Rowan, M., Narayan, R., Johnson, M., & Sironi, L. 2018, MNRAS, 478, 5209
Chael, A. A., Johnson, M. D., Narayan, R., et al. 2016, ApJ, 829, 11
Chan, C.-K., Psaltis, D., Özel, F., Narayan, R., & Sadowski, A. 2015, ApJ, 799, 1
Cho, I., Jung, T., Zhao, G.-Y., et al. 2017, PASJ, 69, 87
Coles, W. A., Harmon, J. K., & Martin, C. L. 1991, JGR, 96, 1745
Coles, W. A., Rickett, B. J., Codona, J. L., & Frehlich, R. G. 1987, ApJ, 315, 666
Cordes, J. M., & Lazio, T. J. W. 1997, ApJ, 475, 557
Davelaar, J., Mościbrodzka, M., Bronzwaer, T., & Falcke, H. 2018, A&A, 612, A34
Davies, R. D., Walsh, D., & Booth, R. S. 1976, MNRAS, 177, 319
Deller, A. T., Brisken, W. F., Phillips, C. J., et al. 2011, PASP, 123, 275
Desvignes, G., Eatough, R. P., Pen, U. L., et al. 2018, ApJL, 852, L12
Dexter, J., Agol, E., Fragile, P. C., & McKinney, J. C. 2010, ApJ, 717, 1092
Dexter, J., Deller, A., Bower, G. C., et al. 2017, MNRAS, 471, 3563
Doeleman, S. S., Shen, Z.-Q., Rogers, A. E. E., et al. 2001, AJ, 121, 2610
Doeleman, S. S., Weintroub, J., Rogers, A. E. E., et al. 2008, Natur, 455, 78

Eatough, R. P., Falcke, H., Karuppusamy, R., et al. 2013, Natur, 501, 391
Falcke, H., & Markoff, S. 2000, A&A, 362, 113
Fish, V. L., Doeleman, S. S., Beaudoin, C., et al. 2011, ApJL, 727, L36
Fish, V. L., Johnson, M. D., Doeleman, S. S., et al. 2016, ApJ, 820, 90
Fish, V. L., Johnson, M. D., Lu, R.-S., et al. 2014, ApJ, 795, 134
Gold, R., McKinney, J. C., Johnson, M. D., & Doeleman, S. S. 2017, ApJ, 837, 180
Goldreich, P., & Sridhar, S. 1995, ApJ, 438, 763
Goldreich, P., & Sridhar, S. 2006, ApJL, 640, L159
Goodman, J., & Narayan, R. 1989, MNRAS, 238, 995
Gravity Collaboration, Abuter, R., Amorim, A., et al. 2018, A&A, 615, L15
Greisen, E. W. 2003, ASSL, 285, 109
Gwinn, C. R., Bartel, N., & Cordes, J. M. 1993, ApJ, 410, 673
Gwinn, C. R., Kovalev, Y. Y., Johnson, M. D., & Soglasnov, V. A. 2014, ApJL, 794, L14
Gwinn, C. R., Popov, M. V., Bartel, N., et al. 2016, ApJ, 822, 96
Han, J. L., Manchester, R. N., Lyne, A. G., Qiao, G. J., & van Straten, W. 2006, ApJ, 642, 868
Iroshnikov, P. S. 1964, SvA, 7, 566
Johnson, M. D. 2016, ApJ, 833, 74
Johnson, M. D., Fish, V. L., Doeleman, S. S., et al. 2015, Sci, 350, 1242
Johnson, M. D., & Gwinn, C. R. 2015, ApJ, 805, 180
Johnson, M. D., Kovalev, Y. Y., Gwinn, C. R., et al. 2016, ApJL, 820, L10
Johnson, M. D., & Narayan, R. 2016, ApJ, 826, 170
Kim, J., Marrone, D. P., Chan, C.-K., et al. 2016, ApJ, 832, 156
Kino, M., Niinuma, K., Zhao, G.-Y., & Sohn, B. W. 2015, PKAS, 30, 633
Kraichnan, R. H. 1965, PhFl, 8, 1385
Kravchenko, E. V., Cotton, W. D., Yusef-Zadeh, F., & Kovalev, Y. Y. 2016, MNRAS, 458, 4456
Krichbaum, T. P., Graham, D. A., Witzel, A., et al. 1998, A&A, 335, L106
Krichbaum, T. P., Zensus, J. A., Witzel, A., et al. 1993, A&A, 274, L37
Lambert, H. C., & Rickett, B. J. 1999, ApJ, 517, 299
Lazio, T. J. W., & Cordes, J. M. 1998, ApJ, 505, 715
Lewandowski, W., Dembska, M., Kijak, J., & Kowalińska, M. 2013, MNRAS, 434, 69
Lo, K. Y., Shen, Z.-Q., Zhao, J.-H., & Ho, P. T. P. 1998, ApJL, 508, L61
Löhmer, O., Kramer, M., Mitra, D., Lorimer, D. R., & Lyne, A. G. 2001, ApJL, 562, L157
Lu, R.-S., Krichbaum, T. P., Eckart, A., et al. 2011, A&A, 525, A76
Lu, R.-S., Krichbaum, T. P., Roy, A. L., et al. 2018, ApJ, 859, 60
Mościbrodzka, M., Gammie, C. F., Dolence, J. C., Shiokawa, H., & Leung, P. K. 2009, ApJ, 706, 497
Mościbrodzka, M., Shiokawa, H., Gammie, C. F., & Dolence, J. C. 2012, ApJL, 752, L1
Narayan, R. 1992, RSPTA, 341, 151
Narayan, R., & Goodman, J. 1989, MNRAS, 238, 963
Neugebauer, M. 1975, JGR, 80, 998
Ortiz-León, G. N., Johnson, M. D., Doeleman, S. S., et al. 2016, ApJ, 824, 40
Özel, F., Psaltis, D., & Narayan, R. 2000, ApJ, 541, 234
Pilipenko, S. V., Kovalev, Y. Y., Andrianov, A. S., et al. 2018, MNRAS, 474, 3523
Psaltis, D., Narayan, R., Fish, V. L., et al. 2015a, ApJ, 798, 15
Psaltis, D., Özel, F., Chan, C.-K., & Marrone, D. P. 2015b, ApJ, 814, 115
Psaltis, D., Johnson, M., Narayan, R., et al. 2018, ApJ, submitted (arXiv:1805.01242)
Pu, H.-Y., Akiyama, K., & Asada, K. 2016, ApJ, 831, 4
Rickett, B., Johnston, S., Tomlinson, T., & Reynolds, J. 2009, MNRAS, 395, 1391
Rickett, B. J. 1990, ARA&A, 28, 561
Shen, Z.-Q., Lo, K. Y., Liang, M.-C., Ho, P. T. P., & Zhao, J.-H. 2005, Natur, 438, 62
Sicheneder, E., & Dexter, J. 2017, MNRAS, 467, 3642
Smirnova, T. V., & Shishov, V. I. 2010, ARep, 54, 139
Spangler, S. R., & Gwinn, C. R. 1990, ApJL, 353, L29
Spitler, L. G., Lee, K. J., Eatough, R. P., et al. 2014, ApJL, 780, L3
Sridhar, S., & Goldreich, P. 1994, ApJ, 432, 612
Tatarskii, V. I. 1971, The Effects of the Turbulent Atmosphere on wave Propagation (Jerusalem: Israel Program for Scientific Translations)
Thompson, A. R., Moran, J. M., & Swenson, G. W., Jr. 2017, Interferometry and Synthesis in Radio Astronomy (3rd ed.; New York: Springer)
Yuan, F., & Narayan, R. 2014, ARA&A, 52, 529
Yuan, F., Quataert, E., & Narayan, R. 2003, ApJ, 598, 301
Zhao, G.-Y., Kino, M., Cho, I.-J., et al. 2017, in IAU Symp. 322, The Multi-messenger Astrophysics of the Galactic Centre, ed. R. M. Crocker, S. N. Longmore, & G. V. Bicknell (Cambridge: Cambridge Univ. Press), 56